Journal of Orthopaedic Translation 48 (2024) 70–88

Contents lists available at ScienceDirect

Journal of Orthopaedic Translation

journal homepage: www.journals.elsevier.com/journal-of-orthopaedic-translation

Original Article

Structure, ingredient, and function-based biomimetic scaffolds for accelerated healing of tendon-bone interface

YuHan Dong [a,1], JiangFeng Li [b,1], Qiang Jiang [a], SiRong He [c], Bin Wang [d], QiYing Yi [e], XiTing Cheng [a], Xiang Gao [f], Yan Bai [a,*]

[a] College of Pharmacy, Chongqing Medical University, Chongqing, 400016, China
[b] Institute of Burn Research, Southwest Hospital & State Key Lab of Trauma, Burn and Combined Injury, Third Military Medical University (Army Medical University), Chongqing, 400038, China
[c] School of Basic Medicine, Chongqing Medical University, Chongqing, 400016, China
[d] Institute of Life Sciences, Chongqing Medical University, Chongqing, 400016, China
[e] Laboratory Animal Center, Chongqing Medical University, Chongqing, 400016, China
[f] College of Stomatology, Chongqing Medical University, Chongqing, 400016, China

ARTICLE INFO

Keywords:
Alg/Col-I hydrogel
Biomimetic scaffold
nHA/PLGA scaffold
PLLA oriented fibers
Tendon-bone healing

ABSTRACT

Background: Tendon-bone interface (TBI) repair is slow and challenging owing to its hierarchical structure, gradient composition, and complex function. In this work, enlightened by the natural characteristics of TBI microstructure and the demands of TBI regeneration, a structure, composition, and function-based scaffold was fabricated. *Methods*: The biomimetic scaffold was designed based on the "tissue-inducing biomaterials" theory: (1) a porous scaffold was created with poly-lactic-co-glycolic-acid, nano-hydroxyapatite and loaded with BMP2-gelatin$_{mp}$ to simulate the bone (BP); (2) a hydrogel was produced from sodium alginate, type I collagen, and loaded with TGF-β3 to simulate the cartilage (CP); (3) the L-poly-lactic-acid fibers were oriented to simulate the tendon (TP). The morphology of tri-layered constructs, gelation kinetics, degradation rate, release kinetics and mechanical strength of the scaffold were characterized. Then, bone marrow mesenchymal stem cells (MSCs) and tenocytes (TT-D6) were cultured on the scaffold to evaluate its gradient differentiation inductivity. A rat Achilles tendon defect model was established, and BMSCs seeded on scaffolds were implanted into the lesionsite. The tendon-bone lesionsite of calcaneus at 4w and 8w post-operation were obtained for gross observation, radiological evaluation, biomechanical and histological assessment.
Results: The hierarchical microstructures not only endowed the scaffold with gradual composition and mechanical properties for matching the regional biophysical characteristics of TBI but also exhibited gradient differentiation inductivity through providing regional microenvironment for cells. Moreover, the scaffold seeded with cells could effectively accelerate healing in rat Achilles tendon defects, attributable to its enhanced differentiation performance.
Conclusion: The hierarchical scaffolds simulating the structural, compositional, and cellular heterogeneity of natural TBI tissue performed therapeutic effects on promoting regeneration of TBI and enhancing the healing quality of Achilles tendon.
The translational potential of this article: The novel scaffold showed the great efficacy on tendon to bone healing by offering a structural and compositional microenvironment. The results meant that the hierarchical scaffold with BMSCs may have a great potential for clinical application.

1. Introduction

Tendon-bone interface (TBI) injury is typically caused by trauma, long-term strains, excessive exercise, etc., and is one of the most common musculoskeletal injuries in humans [1]. Natural TBI is highly anisotropic and consists of mechanical, compositional, and hierarchical

* Corresponding author. School of Pharmacy, Chongqing Medical University, District of Yuzhong, Chongqing, fax: 400016, China.
E-mail addresses: baiyan1226@163.com, baiyan@cqmu.edu.cn (Y. Bai).
[1] These authors contributed equally to this work.

https://doi.org/10.1016/j.jot.2024.07.007
Received 25 March 2024; Received in revised form 11 June 2024; Accepted 16 July 2024

structures with tendon and bone-like properties. TBI serves as a special transition area from soft tissues to hard tissues, which consists of four distinct structures (Fig. 1) [2,3]: tendon (I), non-mineralized fibrocartilage (II), mineralized fibrocartilage (III), and bone (IV). Furthermore, TBI achieves musculoskeletal functions due to its unique structure, complex composition, and graded properties. However, it poses significant challenges to regeneration of TBI injuries [4]. Despite numerous therapeutic strategies that have been used to treat tendon injuries, including surgical and conservative treatment modalities, clinical outcomes remain dismal [5]. The lack of a functionally graded transition at the healing interface and filled with poorly disordered neo-fibrovascular scar tissue [6], results in severe stress concentrations because of the structural mismatch between tendon and bone, contributing to high failure rates following surgical repair (22–91 %) [7]. Therefore, a new strategy is necessary for TBI regeneration while preserving the continuous graded structures and distinct characteristics of normal tissues.

Earlier reports have validated the efficacy of biomimetic scaffolds in TBI regeneration, but the reported scaffold still had limitations in representing the complex structure of TBI [8]. Given the complex composition and architecture of the TBI, single biomaterials in TBI tissue engineering do not reflect the structural and gradients of TBI and exhibit poorer performance [9]. In contrast, a combination of different functional materials can leverage the properties of each biomaterial and achieve similar functions to TBI [10]. Some researchers have designed multilayer scaffolds with two or more different phases for TBI regeneration. For example, Li et al. developed a three-dimensional (3D) printed multiphasic support for TBI treatment, adopting a stratified cell-seeding method [11]. However, the existing technology cannot discern the connection among heterogeneous structure, cell, and matrix

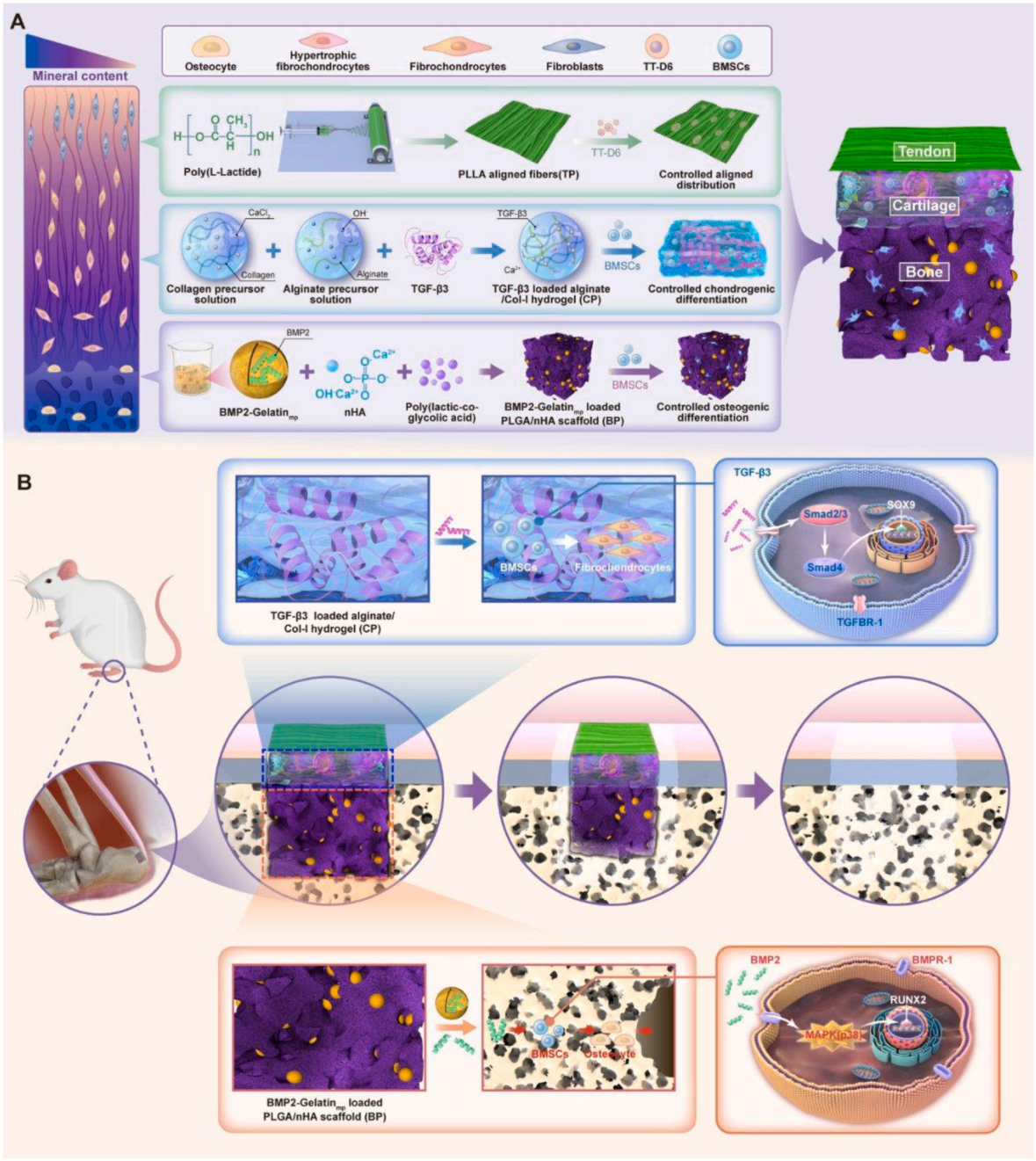

Fig. 1. Schematic demonstrating the fabrication process of the high bionic composite scaffolds for repairing of tendon-bone interface.

components, as well as the mechanical properties or extracellular matrix (ECM) structure of TBI. This is mainly due to the current technical bottleneck and the complex structure and function of natural TBI, and the current multilayer scaffolds still cannot adequately repair and achieve stability at the tissue. Therefore, researching multilayer scaffolds with a natural gradient-like structure while avoiding discrete separation at the interface is necessary.

To simulate the heterogeneous tissue structure of the TBI and better promote its integrated repair, we designed a novel 3D scaffold that can mimic the composition, structure, and mechanical properties of natural TBI. A hierarchical structure was designed based on the TBI, including the bone, fibrocartilage, and tendon phases [9,12–14]. Firstly, to mimic the bone phase, a porous polymer scaffold was fabricated with an architecture based on the type of bone tissues [15,16]. As mechanical support, it simulated the bearing of physical mineralized ECM structure and allowed for cell recruitment and differentiation [17,18]. Secondly, hydrogels were used to simulate the cartilage phase, providing a microenvironment for cell growth, and allowing for the transportation of nutrients and metabolic waste through the elastic network [19]. The hydrogels were composed of a combination of type I collagen (Col-I) and alginate sodium (Alg) due to their biocompatible and biodegradable properties [20,21], simulating the native cartilage ECM and providing a temporary 3D microenvironment for cell proliferation and differentiation [22–24]. Thirdly, anatomically, tendon consist of hierarchically aligned collagen fiber bundles and provide the mechanical strength to withstand tension during physical activity [25–27]. Poly (L-lactic acid) (PLLA) [28–30] was used to prepare the aligned fibers for simulating the tendon phase, which could guide cell elongation along the direction of the aligned fibers [31] and ensure the mechanical integrity of the scaffold during tendon regeneration [32]. In addition to the graded structure, the synthesized scaffold exhibited spatial variations, including cell phenotypes and ECM composition (e.g., growth factors) [33,34]. Previous studies have demonstrated that bone morphogenetic protein (BMP) and transforming growth factor-β (TGF-β) superfamilies were targets for tendon-to-bone tissue and osteochondral tissue regeneration [35]. Regional tissue and region-specific cell phenotypes of TBI tissue were formed by regulating the secretion and spatial distribution of the bioactive factors of the TGF-β and BMP superfamilies [36–38]. The latter performs a variety of functions, including a differentiation stimulator of mesenchymal stem cells for endochondral ossification and osteogenesis [39,40]. On the other hand, the former promotes the proliferation of fibroblasts and osteoblasts, enhancing the healing strength of fibrous tissue, and improving the repair of cartilage and bone [41]. As it was confirmed that TGF-β could facilitate the formation of the cartilage and matrix remodeling in tendon healing by promoting collagen synthesis so as to improve the mechanical strength of the tendon [42–44], and it was also considered to be one of the important factors in promoting scarless healing. Accordingly, including these spatially-regulated biochemical signals into the composite promotes the regional regulation of cell fate, hence achieving bionic engineering scaffolds that are closer to natural tissues.

This study reports the design, fabrication, and evaluation of a hierarchically-structured scaffold that simulates the anatomic structure of the tendon to bone attachment site. Based on the principles of the "tissue-inducing biomaterials" theory, a hierarchically-structured scaffold with a continuous hierarchical was designed, fabricated, and evaluated to promote TBI regeneration, and this study provided a regional microenvironment for cell gradient differentiation, so as to promote the integrated repair of different tissues in the TBI. According to the heterogeneous structure of the TBI, the scaffold material was divided into three regions to provide a more suitable microenvironment for different cell growth and differentiation (Fig. 1): (1) a porous scaffold created with poly lactic-co-glycolic acid and nano-hydroxyapatite (PLGA/nHA), and was loaded with BMP2-gelatin$_{mp}$ to simulate the bone phase of TBI and improve integration of the scaffold with the underlying bone, (2) a hydrogel was created with sodium alginate and type I collagen and loaded with TGF-β3 (Alg/Col-I) to simulate the cartilage phase and promote stress transfer between tendon and bone, (3) oriented PLLA fibers were used to simulate the tendon phase and induce the growth of tenocytes (TT-D6) as well as integration of the scaffold with the tendon. The physicochemical, mechanical, and biological properties of biomimetic scaffolds were investigated, including their effects on tenogenic, osteogenic and chondrogenic differentiation of bone marrow mesenchymal stem cells (BMSCs) *in vitro,* and TBI repair *in vivo*. The results revealed that the biomimetic scaffold not only promoted cell differentiation and TBI regeneration but also achieved specific changes in the TBI heteromorphic matrix and cell population, showing hierarchical mechanical properties and tissue induction properties. Therefore, the composite scaffolds simulating the structural, compositional, and cellular heterogeneity of natural TBI tissue are promising options for the repair of TBI injury.

2. Materials and methods

2.1. Fabrication of the tri-layered scaffold

Fabrication of simulated bone phase (BP): The simulated bone phase scaffold was prepared by particle leaching method by mixing PLGA and nHA with BMP2-loaded gelatin microparticles (BMP2-gelatin$_{mp}$). Briefly, sodium chloride (2.5 g) and nHA (0.1 g) were dispersed in 10 % (w/v) PLGA-chloroform solution and stirred until the mixture was uniformly dispersed. BP_1 (1/3), BP_2 (1/5), and BP_3 (1/9) from PLGA and NaCl were prepared with different mass ratios. Then, BMP2-loaded gelatin microparticles were added to the mushy mixture. The fabrication method of BMP2-gelatin$_{mp}$ in this study was the same as previously described [45]. The mixture was then injected into the scaffold mold and dried for 24 h at room temperature to obtain the nHA/PLGA (NaCl) composite scaffold. After solvent evaporation, the scaffold was carefully washed with distillate water for 2 days until complete salt removal. Finally, the porous scaffold was dried in a blast dryer at 37 °C.

Fabrication of simulated cartilage phase (CP): Alg solutions and Col-I solutions were thoroughly mixed at the same concentration (9.1 mg/mL) on the ice box. Samples were prepared by using Alg and Col-I solutions at different volume ratios and named CP_1 (Alg/Col-I = 6/4), CP_2 (Alg/Col-I = 5/5), and CP_3 (Alg/Col-I = 4/6). The blend was neutralized with 1 M sodium hydroxide until the pH was adjusted to 7.4. Lastly, TGF-β3 solution was added to the mixture and cross-linked by calcium chloride solution, and then put into 37 °C incubator for half an hour to obtain Alg/Col-I hydrogels.

Fabrication of simulated tendon phase (TP): TP was prepared by electrospinning technology. Briefly, PLLA was dissolved in chloroform to achieve a polymer concentration of 8 % (w/v). Ensure that the internal temperature of the machine during operation is 40 °C. The processing parameters were as follows: 25 kV voltage, 0.3 μL/s flow rate, 20 cm tip-to-target distance, and 1500 rpm/min rotating target speed.

Fabrication of composite scaffold with growth factors (simulated Bone/Cartilage/Tendon phase scaffold, BCT@GFs): Fig. 1 illustrates the fabrication of the tri-layered scaffold used in this study. The CP hydrogel precursor solution was applied to the surface of BP, and TP was placed externally by the viscosity of the mixture. Calcium chloride solution (0.1 M) was added into the hydrogel layer for cross-linking, and the BCT@GFs scaffold was obtained after gelation. The same method was used for the preparation of BCT scaffold without adding growth factors.

Fabrication of cells seeded BCT@GFs scaffold (Cells + BCT@GFs): Suspensions of BMSCs and TT-D6 of 1×10^4 cells were separately dripped onto the upper and lower surfaces of the scaffold after the composite scaffold was prepared and freeze-dried. Firstly, the cell suspension of BMSCs was dripped onto the bone and cartilage phases. During the droplet process, BP and CP area were uniformly covered with BMSCs suspensions and without cell aggregation. Subsequently, the scaffold seeded with BMSCs was placed in culture medium to facilitate cell attachment in optimal culture conditions. After the attachment of

BMSCs, the scaffold was flipped, and the same steps were followed to seeded TT-D6 on the TP area.

2.2. Characterization of biomimetic scaffolds

Samples were placed on the sample holder, followed by coating with a thin layer of gold under vacuum by sputter coater at 20 mA, 10^{-1} mbar vacuum. The morphology of the mono-layered and tri-layered constructs was characterized via scanning electron microscopy (SEM). The porosity of BP scaffolds was measured by the liquid displacement method. Meanwhile, the porosity of CP was calculated by SEM and ImageJ software. SEM energy-dispersive X-ray spectroscopy (EDS) mapping operated at 15 kV to perform the element analysis of samples after mineralization. Before being collected, all samples were sputtered with a thin layer of gold for 60 s.

2.3. Gelation kinetics

Oscillatory rheology was applied to pre-gelled hydrogel solutions using a rheometer equipped with a 20 mm parallel plate geometry. Gelation kinetics were analyzed by monitoring storage modulus (G′) and loss modulus (G″) at 37 °C. Strain and oscillatory frequency were kept constant at 0.5 % and 10 rad/s, respectively. After collagen fibrillation, $CaCl_2$ (150 mM) was introduced to trigger ionotropic gelation of Alg solution. This process was also conducted on control samples of Col-I (9.1 mg/mL) and Alg (9.1 mg/mL) separately to acquire the gelation profiles of the raw materials.

2.4. Degradation experiments

After recording the initial weight of the samples, they were immersed in phosphate buffer saline (PBS, pH 7.4) solutions at 37 °C in order to simulate the degradation conditions *in vitro*. At each time point, the samples were washed with distilled water to remove potentially precipitated salts and dried overnight. Samples were weighed and incubated again in fresh PBS. This procedure was repeated once a week.

2.5. Release kinetics of TGF-β3 and BMP2

CP hydrogel and BMP2-$Gelatin_{mp}$ were placed in a centrifuge tube containing 1 mL PBS (pH 7.4). The samples were incubated at 37 °C and centrifuged at 100 rpm. The supernatant was collected at predetermined intervals and stored at −80 °C. Finally, samples were resuspended in 1 mL fresh PBS and incubated to the next time point. The release rates of growth factors were measured using enzyme-linked immunosorbent assay (ELISA) kits.

2.6. Mechanical strength analysis

The mechanical properties of BP scaffolds and CP hydrogels were evaluated by uniaxial unconfined compression test. To minimize measurement errors, uniformly shaped cylindrical samples (diameter: 5 mm, height: 5 mm) were prepared and tested. A strain rate of 0.1 mm/min was applied to samples using a universal testing machine equipped with a 10 N load cell. The compressed Young's modulus was calculated from the slope of the stress–strain curve.

Mechanical properties of the same batch of TP scaffolds with different folding layers were investigated. Samples of TP scaffolds were randomly selected, and the thickness was measured with a vernier caliper and sliced into widths of 10 mm. The tensile test was carried out by an electronic universal tensile tester. Samples were fixed in the fixture of the mechanical tensimeter so that the vertical axis of samples coincided with the center line of the upper and lower fixture. The clamping length and stretching speed were 22 mm/min and 13.2 mm/min, respectively. Finally, tensile strength, average Young's modulus, and maximum tensile strain of fibers were determined from the stress–strain curves.

2.7. Protein adsorption

Bicinchoninic acid (BCA) protein assay kit was used to quantify the amount of protein adsorbed into scaffolds. In this assay, the protein contents of BP, CP, TP, and BCT were measured first, then the protein contents of BCT without BP scaffold (CP + TP) and BCT scaffold without TP membrane (BP + CP) were measured. Scaffolds were incubated in α-minimum essential medium at 37 °C for 6 h, and then the remaining medium was incubated in BCA reagent for 30 min. The absorbance at 562 nm was measured by a microplate Reader. Cells cultured in alpha minimal essential medium (α-MEM) served as the control.

2.8. Cell proliferation and viability

BMSCs and TT-D6 were seeded at a density of 1×10^4 cells per sample. Cells were co-cultured with scaffolds for 2 weeks. At 1st, 4th, 7th, 14th day, cell counting kit-8 (CCK-8) assays were used to assess cell proliferation of different groups according to the instruction. Absorbance at 450 nm was measured by a microplate reader. For cell viability test, after cultivation at 1st, 4th, and 7th day, cells were washed by PBS and the viability was examined using the calcein acetoxymethyl ester (Calcein-AM)/propidium iodide (PI) double stain kit. The live and dead cells were observed under confocal laser scanning microscopy (CLSM).

2.9. Cell morphology and adhesion on biomimetic scaffolds

After cultivation for 3 days and 7 days, cells were fixed with 4 % (w/v) paraformaldehyde for 10 min, rinsed into PBS for 3 times. Then, cells were incubated with Actin-Tracker Green and 4′,6-diamidino-2-phenylindole (DAPI) for staining cytoskeleton and nucleus. CLSM detected the morphology. To observe cell adhesion on scaffolds, after cultivation for 3 days, cells were washed with PBS to remove the unattached cells and fixed in 2.5 % (w/v) glutaraldehyde at 4 °C overnight, then dehydrated, critical-point dried and sputter coated with gold. Cell adhesion ability of all groups was observed by SEM.

2.10. Cell cycle

In our transwell co-culture assay, BMSCs were seeded in the transwell upper chamber (Transwell: BMSCs), and TT-D6 was seeded in the transwell lower chamber (Transwell: TT-D6). After indirect co-culture, cell cycles of the two cells were compared. Then, both BMSCs and TT-D6 were grown on BCT and BCT@GFs, and cell cycle were compared between direct co-culture of cells on scaffolds with growth factor induction and the ordinary culture plates. Treatment was initiated after 7 days of co-culture, cells were harvested and fixed in 70 % (v/v) ethanol at 4 °C overnight. Cells were washed with PBS and incubated with 10 μg/mL RNase and 5 μg/mL PI dye at room temperature. DNA concentrations at different stages of division were measured by flow cytometry.

2.11. Cell migration

BP scaffold and CP hydrogel were put into serum-free medium and extracted at 4 °C for 7 days. The extracts were used to evaluate cell migration. We performed Live cell imaging using an Operetta high-content imaging system equipped with 37 °C and 5 % carbon dioxide (CO_2). Directly after addition of the extracts, microplates were placed into the pre-heated Operetta system and incubated for 30 min. After incubation, digital phase contrast images were acquired at 20 × high NA objective using Operetta's automatic digital phase contrast algorithm. Digital phase contrast images were acquired using a 20 × high numerical aperture (NA) objective for 48 h at imaging intervals of 60 min. Migrating cells were tracked and imaged using automated single-cell tracking algorithm of the Harmony high-content imaging and analysis

software. Cell migration on TP scaffold was observed by staining intracellular actin and nucleus. To quantify cell migration, 3D migration images were reconstructed from laser confocal stack images, and migration depths were calculated from different 3D images by using ImageJ software.

2.12. Alkaline phosphatase (ALP) activity assay

BMSCs were seeded on BCT and BCT@GFs and incubated in osteogenic induction medium (normal medium supplemented with 100 nM dexamethasone, 10 mM β-glycerol phosphate, and 50 μM L-ascorbic acid). After 7th and 14th day, we performed ALP staining with a 5-bromo-4-chloro-3-indolyl phosphate (BCIP)/tetranitro blue tetrazolium chloride (NBT) ALP staining kit. Moreover, to quantify ALP activities, BMSCs were added with 0.1 % (v/v) TritonX-100 solution and placed in 4 °C for 48 h. Cell lysates were centrifuged for 1 min at 13000 rpm/min. Then, 20 μL supernatants were used to evaluate ALP activities. ALP contents were measured by ALP activity kits.

2.13. Alizarin red S (ARS) assay

After cultivation with for 7 and 14 days, BMSCs were fixed with 4 % (w/v) paraformaldehyde, rinsed, stained with ARS for 40 min and observed under microscope. Then ARS-stained cells were extracted using 500 μL mixed solution of acetic acid (1.4 mM) and ethanol (3.4 mM) for 45 min to further quantify the calcium mineralization, and the absorbance was measured at 450 nm with a microplate reader.

2.14. Toluidine blue staining assay

BMSCs were seeded on BCT and BCT@GFs and incubated in chondrogenic induction medium (normal medium supplemented with 10 ng/mL TGF-β3, 10 nM dexamethasone, 50 mg/mL insulin-transferrin-selenium (ITS), 1 mM sodium pyruvate, 1.25 ng/mL BSA, and 50 mg/L L-ascorbic acid). After cultivation with scaffolds for 7 and 14 days, samples were fixed with 4 % (w/v) paraformaldehyde, stained with toluidine blue for 30 min, rinsed, washed by 95 % ethanol, and observed under the microscope.

2.15. Alcian blue colorimetric assay

The content of glycosaminoglycan (GAG) in culture medium was determined by alcian blue method. All cell cultures were taken for testing. Culture medium of 100 μL was taken, 300 μL alcian blue solution was added and placed at room temperature for 60min. The excess dye was washed away. After the precipitation was dissolved, the content of GAG was obtained by colorimetry at 600 nm according to the standard curve.

2.16. Immunofluorescence

To visualize the expression of the bone, cartilage, and tendon related proteins further, the prepared BCT and BCT@GFs were cultured in differentiation medium for 5 days. After gently washing with PBS, the constructs were fixed in 4 % paraformaldehyde, permeabilized with 0.5 % Triton X-100 and blocked with 5 % BSA. Afterwards, the samples were incubated overnight at 4 °C with the primary antibodies of RUNX2, SOX9, and SCX for the BCT and BCT@GFs. After rewarming the next day, the samples were incubated with FITC-conjugated goat anti-mouse IgG secondary antibody for 1 h at room temperature. The cellular nuclei were counterstained with DAPI. All of the samples were observed via CLSM.

2.17. RNA isolation and quantitative real-time polymerase chain reaction (qRT-PCR) analysis

BMSCs were seeded on BCT and BCT@GFs for 7 days. Total RNA was extracted from BMSCs using a kit reagent. Concentration of total RNA was determined spectrophotometrically using a NanoDrop spectrophotometer. qRT-PCR analysis performed under the following cycling conditions: 95 °C for 10 min, followed by 40 cycles of 95 °C for 10 s and 60 °C for 60 s. Data were quantified using the 2-ΔΔCT method. Fold change in the transcript level was calculated using ΔΔCT normalized to control. The primer sequences are listed in Table S1.

2.18. Western blotting (WB) analysis

The protein expression levels were detected by WB on BCT and BCT@GFs groups after 7 days of culture. Total protein was isolated by lysing with lysis buffer containing phenylmethane sulfonyl fluoride (PMSF) on ice. After lysis, the total protein concentration was determined using a Bio-Rad protein assay system. The protein separated through sodium dodecyl sulfate-polyacrylamide gel electrophoresis (SDS-PAGE) and transferred to polyvinylidene fluoride (PVDF) membranes. Membranes were blocked with 5 % nonfat milk solution at room temperature for 2 h and incubated with primary antibodies (anti-p38MAPK, anti-Phospho-p38MAPK, anti-Smad2/3, anti-Phospho-Smad2/3, anti-SOX9, anti-Runx2, and GAPDH) overnight at 4 °C. After washing, membranes were incubated with horseradish peroxidase-conjugated secondary antibodies for 1 h at 37 °C, and incubated with enhanced luminol-based detection reagent prior to exposure. GAPDH gray value for normalization.

2.19. Surgical procedure

Eight-week-old male Sprague–Dawley Rats weight 250–300 g were used in these experiments. All rats were randomized into 4 groups as follows: blank group with unfilled defect, BCT without growth factors implant group (BCT), BCT with growth factors (BCT@GFs) implant group, cells seeded in BCT with growth factors implant group (Cells + BCT@GFs). Normal rats were general anesthesia with sodium pentobarbital (75 mg/kg).

A 0.5 cm longitudinal incision was made on the posterior calcaneus along lateral skin, and calcaneus was carefully exposed. Then one defect (diameter: 1.5 mm, height: 1.5 mm) was created at the calcaneal insertion of Achilles tendon using a drill. After that, the defect was washed with normal saline to help remove blood, broken bone, tissue debris, etc. in the defect area. The scaffold was contacted with the calcaneus with the BP layer inward to fill the bone defect area; The TP layer is outward connected with the Achilles tendon, and the TP layer is partially fixed to the defect free part of the Achilles tendon by 6-0 suture to fix the scaffold. Scaffolds were implanted into the defects, and the blank group was subjected to surgery without scaffold implantation. After that, wounds were carefully sutured and penicillin was intramuscularly injected for 3 days to prevent infection. At postoperative 4th and 8th week, rats were euthanized (overdose by sodium pentobarbital, 100 mg/kg), calcaneus with surrounding soft tissue specimens were observed and stored in 4 % (w/v) paraformaldehyde for further analysis.

2.20. Gross observation and radiological evaluation

At predetermined time points, immediately after the acquisition process, samples of each group were photographed. Afterwards, X-ray and micro computed tomography (micro-CT) analysis were conducted to acquire 2D and 3D images as well as the relative bone volume fraction (BV/TV), relative bone surface fraction (BS/TV), and bone mineral density (BMD) of each sample.

2.21. Biomechanical analysis

The specimens were used for mechanical tensile testing. The cross-sectional area of calcaneus and its surrounding soft tissue enthesis were measured by a digital caliper. CellScale UniVert system performed the uniaxial tensile tests. A movement rate of 0.05 mm/s was administered to each specimen until failure.

2.22. Histological assessment

Specimens were decalcified using 10 % (w/v) ethylenediaminetetraacetic acid (EDTA) in PBS for 1 m, and embedded in paraffin. Then, each paraffin block was sliced into 5 μm thick sections, stained with hematoxylin and eosin (H&E) to assess morphology and inflammatory changes and *in vivo* degradation. H&E images could roughly be defined as the degraded scaffold, and the non-degraded scaffold. The degradation rate (%) = (the degraded scaffold area/the entire repair tissue area) × 100 %, where the area was measured by ImageJ software.

The sections were also stained with Masson's trichrome (MT) and safranin-O/fast green (SO/FG) to examine collagen production, chondrogenesis, and osteogenesis. Healing of the reconstructed enthesis was assessed via a tendon maturing scoring system as previously described by Ide et al. (Table S2) [46].

2.23. Statistical analysis

Data are expressed as means ± standard deviation for n = 3. Statistical analyses were performed using IBM SPSS software. One-way analysis of variance (ANOVA) was used to assess statistical significance of results. When the variances were homogeneous, LSD, Tukey and Bonferroni tests were used as post hoc tests. Tamhane's T2, Dunnett's T3, and Games–Howell tests were used when the variances were unequal. Thresholds for significance were: ns > 0.05, *$p < 0.05$, **$p < 0.01$ and ***$p < 0.001$. In all the statistical evaluation, a p-value <0.05 was considered as statistically significant.

3. Results and discussions

3.1. Fabrication and characterization of biomimetic scaffolds

Given the graded structure and composition of the native TBI tissue, reflecting the reconstruction of this multi-tissue interface remains a current scientific challenge. For compliance with anatomical features, each biomaterial was localized to a corresponding phase, resulting in the successful fabrication of a biomimetic scaffold. The innovation of this study lay in the preparation of composites with different structural composition, physicochemical properties and regenerative ability through different design and fabrication methods, which used a scaffold, seed cells, and cytokine mediated strategy as a system for overall design of TBI reconstruction from various aspects. Fig. 2A illustrates the structure of the BCT composite scaffold. The morphology of the tri-layer biomimetic scaffold was observed via scanning electron microscope (SEM). The three layers of the scaffolds were clearly identified in Fig. 2B. SEM images displayed that the large surface area of BP enabled uniform distribution of nHA within the materials, which was confirmed by the SEM and energy dispersive spectroscopy (EDS) mapping analysis of a fractured cross-section (Fig. 2C and D). The magnified observation revealed that BMP2 loaded gelatin microparticles (BMP2-gelatin$_{mp}$) and nHA were successfully incorporated into the PLGA matrix, and the surface roughness was significantly enhanced compared to pure PLGA scaffolds (Fig. 2E–S1A-C). On the one hand, the incorporation of nHA could influence the attachment, proliferation, differentiation, and ECM production of BMSCs by improving the roughness and mechanical properties of PLGA scaffolds [47,48]. On the other hand, nHA improved the osteogenic activity of scaffolds owing to its favorable osteoconductivity and osteoinductivity [49], and it was expected to gradually release calcium and phosphorus ions through nHA in bone phase scaffold, and infiltrate into hydrogel to simulate mineralized fibrocartilage. SEM images also displayed that BP possessed excellent macropore connectivity (Fig. 2C), and the porosity and pore diameter of the scaffold were enhanced with an increase in porogen quantity (Fig. S1D-F**)**. The results indicated that the prepared scaffolds met the requirements of engineering bone scaffolds for large pore size (at least 50 μm) and high porosity (approximately 80 %) (Fig. 2C and F) [50].

Both high porosity and interconnection play a crucial role in cell behavior, such as adhesion, infiltration, and migration, as well as the transportation of oxygen, nutrients, and waste [51]. For the cartilage phase, CP scaffolds exhibited a 3D interconnected porous microstructure as well as 40–60 % porosity (Fig. 2G and H, S1G-I). The macroporous nature of Alg/Col-I hydrogels promoted cell penetration and attachment to maintain the homogeneity of the cell-material construction. For the tendon phase, nano-scale pores were observed in PLLA fibers (Fig. 2I), which were beneficial for cellular adhesion. PLLA fibers were highly oriented, with an average diameter of 3.57 ± 0.38 μm; the majority of the fibers in the TP were parallel to each other and formed angles ranging from 0° to 10°with respect to the horizontal axis (Fig. 2J and K). Size of PLLA fibers was consistent with the dimensions of collagen fascicles and the anatomy of the tendon. Therefore, the directional spatial arrangement could guide the direction of tenocytes growth and induce cell infiltration and collagen deposition, thereby promoting the regeneration of the natural tendon structure.

3.2. Degradation, drug release and mechanical properties of biomimetic scaffolds

The degradation rate of scaffolds was studied in the phosphate buffered saline (PBS) solution by immersion experiments. As depicted in Fig. 3A, BP scaffolds were gently degraded within 15 weeks. After soaking for 13 weeks, the degradation rate of BP scaffolds was substantially improved and the mass loss was accelerated. Weight loss rates of BP_1, BP_2, BP_3 were 16.65 ± 5.20, 10 ± 2.07, and 8.32 ± 1.12 %, respectively. At the week 21st, BP scaffolds collapsed and weight loss rates were about 4.81, 5.87, and 4.40 times that at the 13th week. The degradation of each sample was rapid in 1 week and gradually slowed down over 1–4 weeks, Fig. 3B delineated that the weight loss of CP scaffolds increased with an increase in hydrolysis time, and Alg hydrogels (CP_{ALG}) degraded slower than hydrogels containing both Alg and Col-I ($CP_{1\text{-}3}$). These results implied that Alg cross-linked with Col-I hydrogels were resistant to enzymatic degradation compared with Col-I hydrogels, and that cross-linking between Alg and Col-I protected the collagen-based material from enzymatic degradation. The degradation of TP scaffolds is shown in Fig. 3C, with a weight loss rate of TP scaffolds of 27.04 ± 2.82 % after 21 weeks of degradation. The degradation of composite BCT scaffolds showed a decreasing trend and reached 56.77 ± 5.31 % in the 21st week (Fig. 3D). Interestingly, the degradation rate of scaffolds with PLLA fibers was significantly lower than scaffolds without PLLA fibers. PLLA-oriented fibers might limit the contact of lysozyme with the composite scaffolds, which would be beneficial for keeping the structural integrity of scaffolds to match the slow regeneration of the tendon *in vivo*. The *in vitro* degradation of BCT scaffold showed that the scaffold could maintain its integrity before the degradation of TP layer, since the adhesion between the TP layer and the CP layer is attributed to the significant hydrogen bonding forces between the two interface bonding layers.

Controlling the concentration and release rate of functional factors is crucial for regulating the intensity of cellular signaling and biological responses. Delivering growth factors to target sites significantly promotes cell differentiation and tissue regeneration [52,53]. Therefore, the ability of tissue-engineered scaffolds to induce tissue regeneration could be further improved by loading proper growth factors into scaffolds. BMP2 is one of the growth factors with the strongest osteogenic

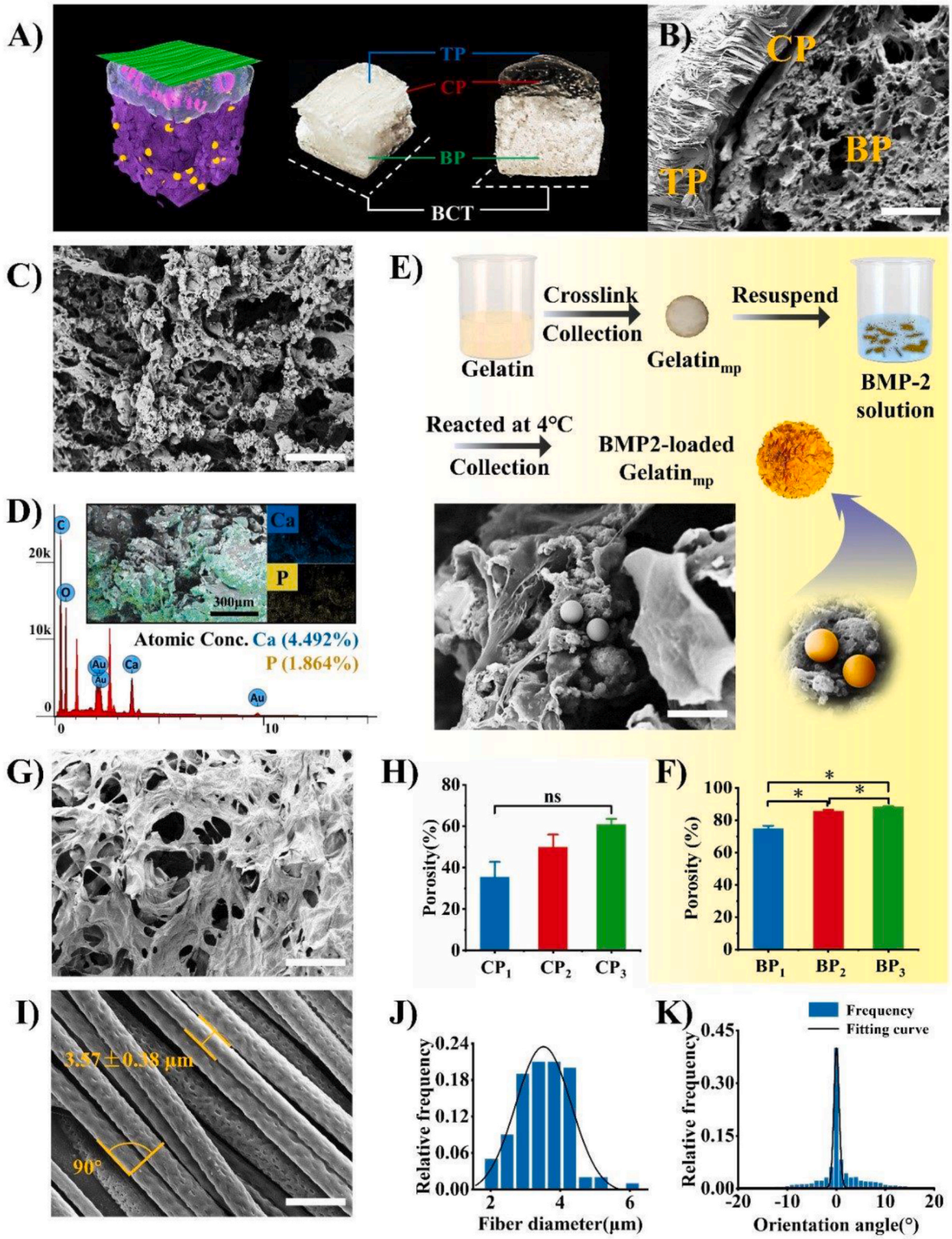

Fig. 2. Morphology characterization of the biomimetic scaffolds. (A) Schematic illustration for the structure of BCT composite scaffolds. **(B)** Different areas showing cross-section of the developed construct focusing on the different sections viz BP scaffolds, CP scaffolds, and outer TP scaffolds (c), Scale bar: 500 μm. **(C)** The morphology of BP scaffolds (simulated bone phase, PLGA/nHA scaffold) with BMP-2 loaded gelatin microspheres, Scale bar: 150 μm. **(D)** SEM image and element diagram of BP scaffolds. **(E)** Fabrication and morphology of BMP-2 loaded gelatin microspheres (Gelatin$_{mp}$) in BP scaffolds, Scale bar: 20 μm. **(F)** The porosity of BP scaffolds prepared with different mass ratio of PLGA to NaCl (BP$_1$:1/3, BP$_2$:1/5, BP$_3$:1/9). **(G)** The morphology of CP scaffolds (simulated cartilage phase, alginate-collagen hydrogel), Scale bar: 300 μm. **(H)** Porosity of CP scaffolds prepared with different volume ratio of sodium alginate to Col-I (CP$_1$:6/4, CP$_2$:5/5, CP$_3$:4/6). **(I)** Morphology of TP scaffolds (simulated tendon phase, PLLA fibrous), Scale bar: 15 μm. **(J, K)** Statistical analysis of distribution of fibers direction and diameter. The curves were fitted with a Gaussian curve. Each data point represented the mean ± standard deviation (n = 3), statistically significant differences were indicated as ns > 0.05, *p < 0.05.

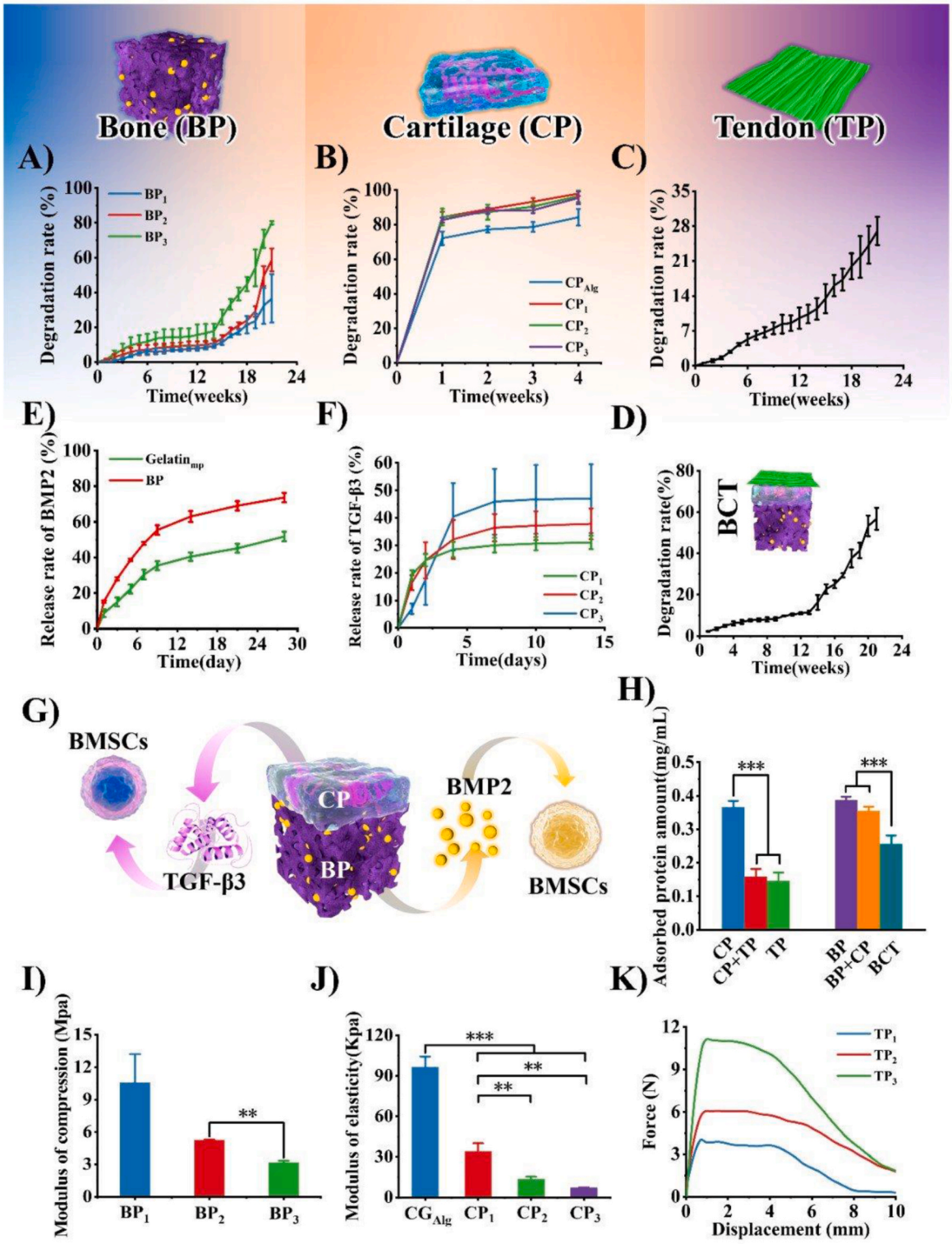

Fig. 3. Characterization of the biomimetic scaffolds. **(A–C)** Degradation of BP, CP, TP, and BCT scaffolds. **(D)** Degradation of BCT scaffolds. **(E)** Release of BMP2 from gelatin$_{mp}$ and BP scaffolds loaded with gelatin$_{mp}$. **(F)** Release of TGF-β3 from CP scaffolds. **(G)** Schematic illustration for growth factor releasing from BP and CP scaffolds. **(H)** Protein adsorption of scaffolds after 6 h. **(I)** Compressive modulus diagram of BP scaffolds. **(J)** Elastic modulus diagram of CP scaffolds. **(K)** Load-displacement diagram of TP scaffolds. BP: scaffolds prepared with different mass ratio of PLGA to NaCl (BP$_1$:1/3, BP$_2$:1/5, BP$_3$:1/9); CP: hydrogels prepared with different volume ratio of sodium alginate to Col-I (CP$_1$:6/4, CP$_2$:5/5, CP$_3$:4/6); TP: PLLA fibrous. Each data point represented the mean ± standard deviation (n = 3), statistically significant differences were indicated as $^{**}p < 0.01$ and $^{***}p < 0.001$.

effects, which plays a key role in most bone-regeneration strategies because of its high osteoinductive potential [54]. Meanwhile, TGF-β3 can induce endochondral osteogenesis and play an anti-fibrotic role through negative feedback effects [55]. Since BMP2 is expressed throughout fracture healing and TGF-β3 is expressed in the early stages of TBI injury [56–58], BMP2 was encapsulated in gelatin$_{mp}$ to prolong the release period. BMP2-gelatin$_{mp}$ was loaded in nHA/PLGA scaffolds, followed by the loading of TGF-β3 into hydrogels by self-assembly technology, achieving a sequential release pattern with initial TGF-β3 releases followed by BMP2. *In vitro* release of BMP2 from gelatin$_{mp}$ and BP scaffolds loaded with BMP2-gelatin$_{mp}$ for 4 weeks is shown in Fig. 3E. BMP2 released from BP scaffolds exhibited a lower initial burst within 1 day (about 8.7 %) and a more sustained release pattern (about 73.6 %) compared with BMP2-gelatin$_{mp}$ (about 52.7 %) for 28 days. The gelatin$_{mp}$ were used as a sustained-release carrier for BMP2, and the total release amount for 28 days was 37.79 ng/mL, which was beneficial for avoiding excessive doses and toxic side effects, meanwhile prolonging the action time of BMP2 and enhancing its therapeutic effects. As demonstrated in Fig. 3F, TGF-β3 released from CP scaffolds presented a fast release. The cumulative release rate of TGF-β3 from CP_1, CP_2, and CP_3 scaffolds was 46.96, 37.81 and 33.27 % on the 14th day, showing a gradually flattened trend and a slow-release rate. These results signaled that a moderate, sustained release of TGF-β3 from CP scaffolds was achieved. BMP2 and TGF-β3 were loaded into corresponding phases of the composite scaffold, thereby realizing controlled and localized delivery of key growth factors from a multifunctional delivery system, and accurately simulating the expression axiom of these growth factors during TBI repair, which could promote cell proliferation and differentiation in a spatially and temporally controlled manner, thereby providing strategies for promoting tissue repair.

Protein adsorption exerts a major impact on the rapid adhesion and spread of cells on the surface of scaffolds. As shown in Fig. 3H, the amount of adsorbed protein of BP, CP and TP scaffolds were 0.39 ± 0.01, 0.15 ± 0.02, and 0.16 ± 0.02 mg/mL, respectively. Protein adsorption capacity of BP + CP composite scaffolds was 0.35 ± 0.01 mg/mL, while that of the BCT composite scaffold was decreased to 0.26 ± 0.02 mg/mL, which might result in a decrease in the number of cells adhering to the external PLLA fibers. The low protein adsorption of BCT composite scaffolds might result lead to decreased adhesion and recruitment of fibroblasts and macrophages, which further minimize fibrosis of tendon tissue.

TBI participates in carrying and transferring load to surrounding tissues. Thus, tissue-engineered scaffolds need to simulate the mechanical properties of different phases in multi-tissue interfaces. The designed scaffolds are expected to solve the mechanical differences between different tissues and achieve better repair. To address the stiffness mismatch among bone, cartilage and tendon tissues, a hierarchically-structured composite materials with different stiffness in each layer was designed to simulate the structure and composition of the TBI as much as possible for better matching the mechanical properties of the surrounding tissues. Therefore, the mechanical properties of the scaffold with different component ratios were explored as screening conditions for the final constructs. For the bone phase, studies showed that the required compressive strength of bones in different parts of the human body ranged from 4.0 to 12.0 MPa [59]. BP_1 exhibited a mechanical strength of 10.53 ± 2.67 MPa that approximated bone tissues (Fig. 3I). For the simulated cartilage phase, cross-links between Col-I and Alg in hydrogels improved mechanical stability and offered a favorable environment for cells (Fig. S2). Moreover, CP_1 scaffolds showed the highest compressive strength (34.12 ± 5.94 KPa) among all CP scaffolds (Fig. 3J), which indicated that addition of Alg improved the compressive strength of Col-I hydrogels, thereby providing a mechanical support for cell proliferation and differentiation. The modulus of the BP scaffold was about 10 MPa, whereas that of the CP scaffold was about 34 KPa. Such a mechanical strength-graded interface was promising for dissipating stress concentrations between two dissimilar tissues and reproduced a critical feature of the natural TBI. Representative load–displacement curves of TP scaffolds are shown in Fig. 3K. In the membrane thickness range of 27–78 μm, the maximum load of PLLA fibers was 4.33 ± 0.32 to 11.31 ± 0.48 N, which demonstrated that the maximum load of PLLA fibers could meet the criteria for tendon repair. These results indicated that the tri-layers biomimetic scaffold could simulate the natural structure of the ECM of the TBI cells, meeting the needs of TBI repair. By determining the density, proportion and distribution of components, as well as the concentration and release rate of functional factors in each part of the scaffold, we can control and regulate the structure and function of the tendon bone interface. This regulation is crucial for promoting the repair and reconstruction of the tendon bone interface. In scaffold design, appropriate density selection can affect cell invasion and tissue repair, and provide appropriate cellular environment and nutrient supply. The proportion and distribution of components play an important role in the biocompatibility, mechanical properties, and biological activity of materials. By selecting the appropriate proportion of ingredients, appropriate material mechanical properties can be provided, and cell adhesion and functional differentiation can be promoted.

3.3. BMSCs and TT-D6 growth in biomimetic scaffolds

BMSCs were seeded on the BP and CP scaffolds, TT-D6 was seeded on the TP scaffolds, and cells cultured in plates were used as the control to assess the distribution and proliferation of cells inside the scaffold, as shown in Fig. 4A. Concurrently, the proliferation ratio of BMSCs cultured on BP and CP scaffolds was significantly enhanced with a prolonged culture time, as displayed in Fig. 4B. The proliferation ratios on the 7th day were 25.63 ± 1.34 times and 18.97 ± 4.90 times higher than on the 1st day, respectively. On the 14th day, the proliferation ratio of BMSCs cultured on CP scaffolds was significantly increased, which was 103.45 ± 16.79 times that of control group. These results suggested that BP and CP scaffolds remarkably promoted BMSCs proliferation. Moreover, as shown in Fig. 4C, the proliferation ratio of TT-D6 cultured on TP scaffolds on the 7th day and 14th day was 30.99 ± 1.64 and 43.22 ± 1.88 times that of the control group, respectively. Cell-cycle analysis further revealed that both the direct co-culture group (cells seeded in scaffolds) and the indirect co-culture group (cells seeded in Transwell) significantly increased the cell proportion of the S-phase, and decreased the proportion of G0/G1 phase compared with the control group (Fig. S3). S-phase fraction is the most essential index reflecting the characteristics of cell proliferation and is the gold index representing cell proliferation. An increase in the proportion of cells in S-phase represents an increase in the number of cells entering the material preparation process and indirectly represents a greater number of cells undergoing division. Meanwhile, results of real-time measurements of BMSCs growth via live cell workstation indicated that BMSCs proliferation of both BP scaffolds and CP scaffolds was higher than that of the control group, and cells were evenly distributed (Fig. S4). Altogether, these results indicated that the scaffolds had no cytotoxicity and significantly promoted cell proliferation. Furthermore, the results suggested that the tri-layers biomimetic scaffold could synergistically promote the proliferation of both BMSCs and TT-D6 in distinct support layers.

Live/dead staining results (Fig. 4D and S5**)** displayed that after 7 days of cultivation, the living/dead cells ratio of BMSCs cultured on BP and CP scaffolds was 14.26, 45.10, respectively, and TT-D6 cultured on TP scaffolds was 22.41, represented a high degree of survival of adherent cells. The large amounts of adherent living cells with normal features indicated the BCT scaffolds supported the normal growth of BMSCs and TT-D6, mainly attributing to good interconnectivity and uniformity of scaffolds, allowing efficient exchange of nutrients, oxygen and metabolite wastes.

When cells initially adhered to the surface of materials, they sensed and responded to the surrounding microenvironment, resulting in alterations in their morphology. According to Fig. 4E, BMSCs and TT-D6 adhered on the surface of BP, CP, TP and BCT composite scaffolds

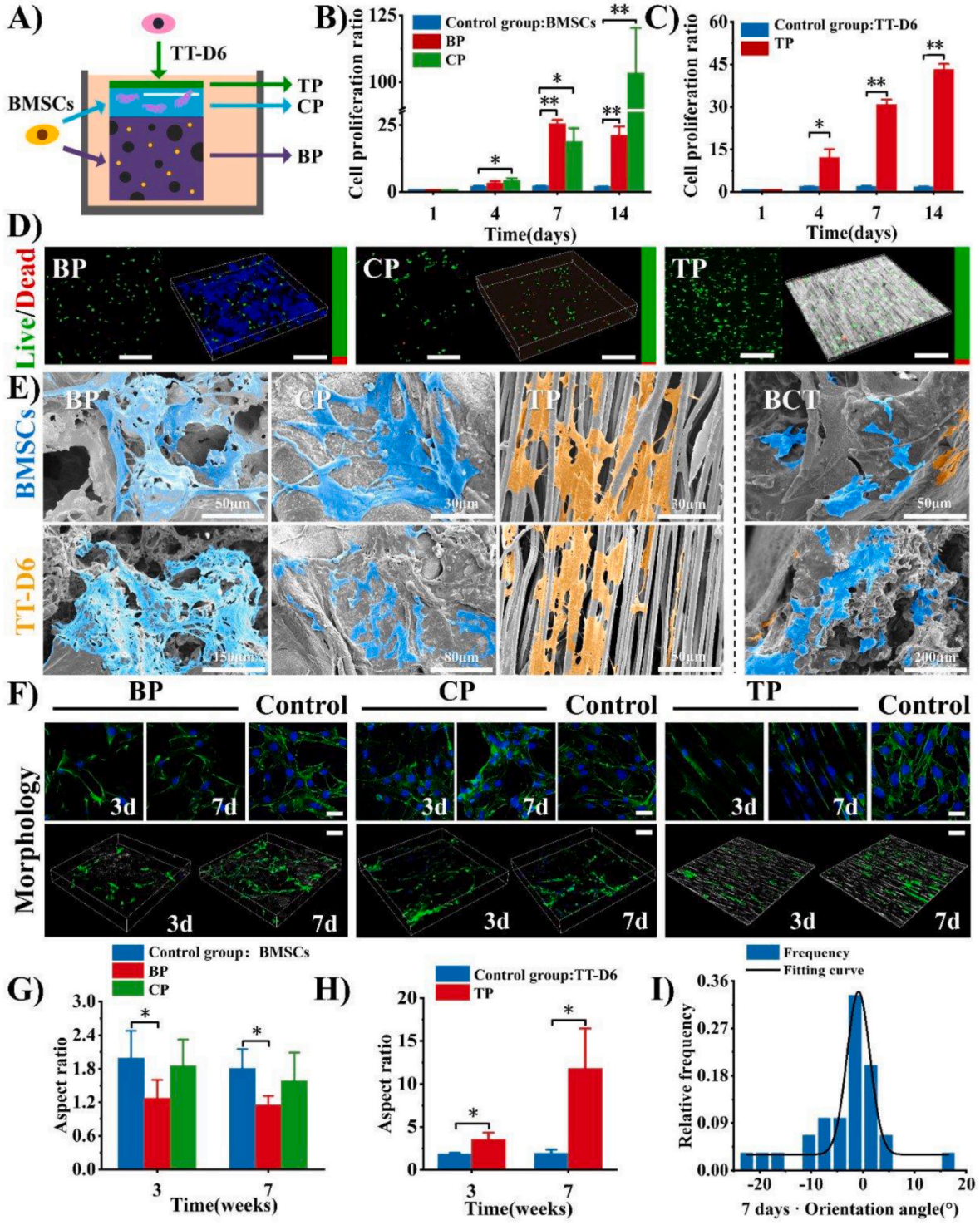

Fig. 4. Cell growth on the biomimetic scaffolds. **(A)**Schematic illustration for experiments of cell growth in tri-layers scaffolds. **(B)** The proliferation ratio of BMSCs cultured in plates (control), BP and CP scaffolds. **(C)** The proliferation ratio of TT-D6 cultured in plates (control) and TP scaffolds. **(D)** Representative 2D and 3D images of BMSCs seeded in BP and CP scaffolds, and TT-D6 seeded in TP scaffolds stained with Calcein-AM (live cells, green fluorescence) and PI (dead cells, red fluorescence) at 7th day after cell seeding. Scale bar: 200 μm (2D images) and 100 μm (3D images). **(E)** SEM images of BMSCs and TT-D6 attachment on BP, CP, TP and BCT scaffolds after co-cultured for 4 days (The blue area is BMSCs and the yellow area is TT-D6). **(F)** Representative 2D images and 3D reconstruction images of BMSCs and TT-D6 stained with DAPI (nucleus, blue fluorescence) and actin-tracker green (actin filaments, green fluorescence) after 3 days and 7 days of co-cultured with BP, CP, and TP scaffolds. Scale bar: 100 μm. **(G, H)** The aspect ratio of BMSCs cultured on BP, CP scaffolds, and TT-D6 cultured on TP scaffolds for 3 days and 7 days. **(I)** Statistical analysis of the distribution of cell direction at 7th day after cell seeding, the curves were fitted with a Gaussian curve. Each data point represented the mean ± standard deviation (n = 3), statistically significant differences were indicated as *p < 0.05 and **p < 0.01.

with complete morphology and evenly sprea d. Fig. 4F–and S6 display the cell behavior and distribution in monophasic structures. Compared to BMSCs cultured on plates, BP scaffolds with a stiffer surface induced BMSCs to exhibit an isotropic star-shaped distribution, with a roundness and aspect ratio of 1.15 ± 0.17 % and 0.85 ± 0.078 % on the 7th day, respectively. According to previous reports, BP may promote BMSCs to differentiate into osteoblast [60,61]. CP scaffolds with a moderately stiff surface induced cell morphology between star-shaped and spindle-shaped, with roundness of 1.59 ± 0.50 % on 7th day, potentially causing BMSCs to differentiate into cartilage cells (Fig. 4G). Moreover, TT-D6 cultured on the TP scaffolds for 7 days showed a prolonged spindle-shaped morphology and clear parallel alignment. The roundness and aspect ratio of cells were 11.80 ± 4.64 % and 0.35 ± 0.059 % (Fig. 4H), respectively. Such highly-oriented PLLA fibers could expand the TT-D6 cytoskeleton and induce cells to elongate in a spindle-like pattern parallel to fibers, and subsequently promote tendon repair (Fig. 4I). The change in cell shape suggests a variation in cellular phenotype in response to the local microenvironment of the scaffold owing to its high osteoinductivity and directional tensile stress.

3.4. Migration of BMSCs and TT-D6 in biomimetic scaffolds

The migration of BMSCs and TT-D6 in biomimetic scaffolds was further assessed to evaluate the vitality of cells on scaffolds. A schematic illustration for real-time measurement of BMSCs migration in BP and CP scaffolds through live cell workstation is shown in Fig. 5A, while the migration trajectory of BMSCs is shown in Fig. 5B. The average migration speed, accumulated distance, and displacement of BMSCs on BP and CP scaffolds were both significantly elevated compared with the control group (Fig. 5C–E). These findings may result from the cytocompatibility of the multiple components contained in our designed scaffold. In line with the results reported in the literature [62], protein components such as BMP2 in the scaffold favored migration. Confocal laser scanning microscopy (CLSM) 3D reconstruction was used to detect cell migration on TP. It can be deduced from Fig. 5F that aligned fibers have wider cell distribution and more cells than non-aligned fibers. The migratory distance was analyzed by software: the distance of TT-D6 in aligned PLLA fibers was 41.52 ± 2.05 μm (Fig. 5G), which was evidently higher than that of cells on the non-aligned fibers (27.82 ± 2.87 μm). Besides, aligned PLLA fibers strongly promoted directed TT-D6 migration and growth in contrast to the randomly-oriented fibers. Numerous studies have demonstrated that the topology of scaffolds can mediate various complex physiological activities of cells [63]. The oriented fibers produced traction forces on cell growth, inducing matrix remodeling and further guiding the direction of cell growth and movement *in vitro*. These results demonstrated that on the three phases of the hierarchical scaffold, BMSCs distributed uniformly, proliferated and migrated freely within the porous microstructure. This feature might be advantageous for repairing TBI, since interconnectivity plays a key role in stimulating cell communication and interaction during healing.

3.5. Osteogenic and chondrogenic differentiation of BMSCs on scaffolds

To evaluate the influence of the hierarchical microstructure scaffold on BMSCs differentiation, biological markers for osteogenesis and chondrogenesis were systematically detected to identify the feature of

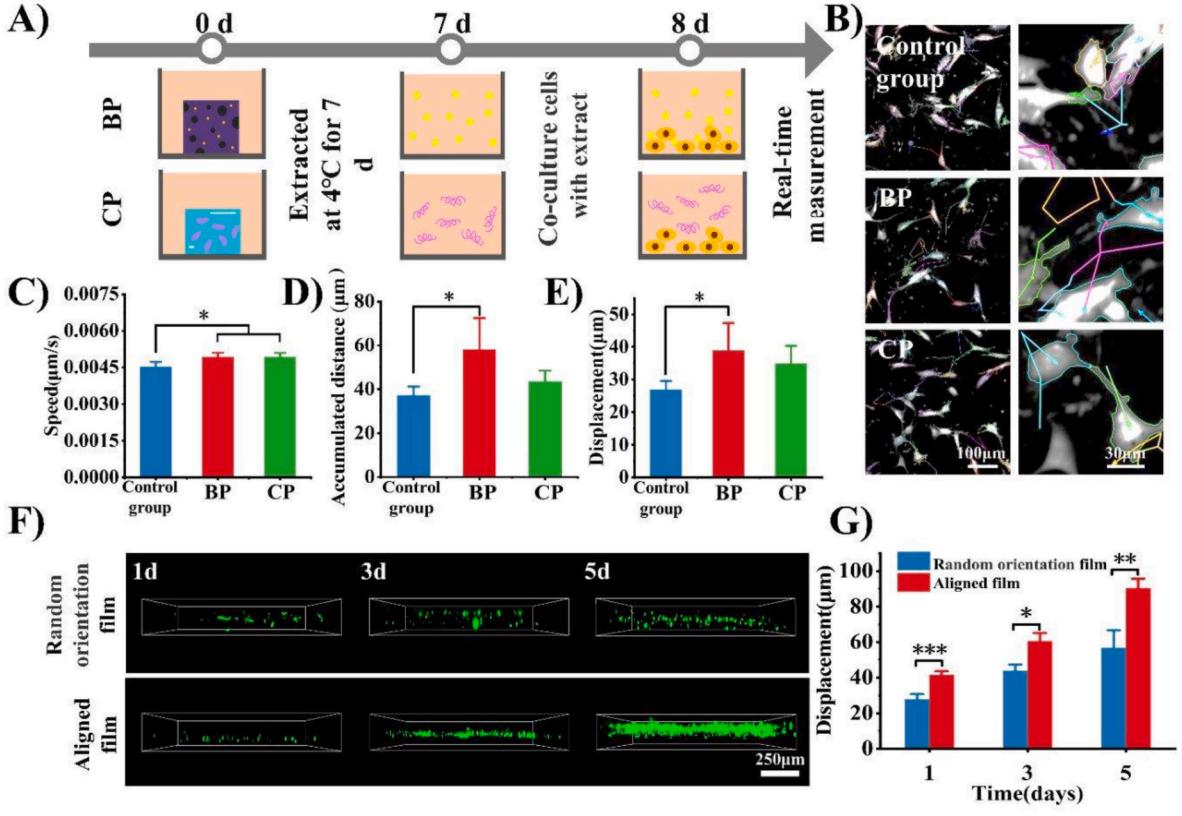

Fig. 5. Cell migration on the biomimetic scaffolds. (A) Schematic diagram of cell migration experiments. BP scaffold and CP hydrogel were put into serum-free medium and extracted at 4 °C for 7 days. The extracts were used to evaluate cell migration. Live cell imaging was performed using an Operetta high-content imaging system equipped with 37 °C and 5 % CO_2. **(B)** Representative migration trajectories of BMSCs cultured in plates, BP and CP scaffolds for 36 h. The right photographs (Scale bar: 30 μm) are the magnified fields of left (Scale bar: 100 μm). **(C–E)** Average speed assay, accumulative distance and displacement of BMSCs migration within 36 h through high content analysis system. **(F)** 3D reconstruction images of TT-D6 migration in TP scaffolds (PLLA oriental film) and un-oriental PLLA film (control). **(G)** Displacement assay of TT-D6 migration in TP scaffolds. Scale bar: 250 μm. Each data point represented the mean ± standard deviation (n = 3), statistically significant differences were indicated as *p < 0.05, **p < 0.01, and ***p < 0.001.

BMSCs differentiation. Osteogenic differentiation of BMSCs on the scaffold was determined by alkaline phosphatase (ALP) and alizarin red S (ARS) assay, and chondrogenic differentiation was determined by toluidine blue staining. As illustrated in Fig. 6A, an increased cell number and darker color were observed in the BCT group in contrast to the control group. Moreover, stronger ALP staining was obviously observed in the BCT@GFs group compared to the control and BCT groups whether on 7th day and 14th day. Fig. 6B and C shows that ALP concentration and activity of BMSCs on BCT@GFs and BCT scaffolds were significantly higher (approximately 9.38 and 1.06 times higher, respectively) than those in the control group ($P < 0.05$). The ARS staining results showed a similar trend as the ALP results. The BCT@GFs group presented larger amounts of calcium nodule deposition on 7th day and 14th day compared to the control and BCT groups (Fig. 6D–F). Along with the addition of BMP2 growth factors, ALP activity and calcium nodule formation of BMSCs seeded on the BCT@GFs scaffold were significantly improved, which further promoted calcium deposition in the bone phase of the composite scaffold. BMSCs have a specific lineage and synthesize a specific matrix based on the matrix's physical microenvironment [64]. These results corroborated that the combination of the topological structure of constructs, BMP2 growth factors, and scaffolds matrix conjointly promoted osteogenic differentiation of BMSCs on the bone phase of the hierarchical scaffold. Osteogenic differentiation of BMSCs could promote the bone formation of TBI defects, which further improved the function of alleviating stress concentration and ultimately promoted biomechanical transduction [65].

The chondrogenic differentiation of BMSCs on the TP hydrogels of the hierarchical scaffold is shown in Fig. 6G–I. After 7 days of chondrogenic induction, toluidine blue staining showed a large heterochromatic matrix and positive toluidine blue staining in the scaffold groups (Fig. 6G). On the 14th day of induction, round-like cells with stratified growth and purplish red heterochromatic particles scattered on the periphery of the cells could be observed in the BCT group, with a higher number of heterochromatic granules in the BCT@GFs group, especially in the stratified growth area; the positive staining area reached 52.54 ± 4.20 % (Fig. 6H). At the same time, on the 7th day, proteoglycan levels in the BCT@GFs group were significantly higher than that in the control group (225.33 ± 5.43 μg/mL) and maintained an increasing trend until the 14th day (Fig. 6I). This suggested that BMSCs differentiated into chondrocytes at an early induction stage, and that more chondrocytes were generated as the induction time increased. As the basic component of hydrogel, Alg has a great impact on the formation of cartilage because it has a structure like cartilage matrix (proteoglycan), which can make chondrocytes grow in a physiological-like state. The reticular structure of hydrogel can also wrap chondrocytes and allow cells to grow in a 3D structure, which aids in maintaining the stability of the cell phenotype and secreting a large amount of ECM. Thus, compared to the control group, TP hydrogels in the hierarchical scaffold presented a superior biological profile of the chondrocytes, with a higher ability to secrete glycosaminoglycan, and facilitated extensive proteoglycan deposition in the BMSCs. These results suggested that the biomimetic scaffold with a hierarchical structure was able to stimulate local stem cell differentiation and that the process was highly dependent on the local compositions and structural features of the scaffold.

Subsequently, to examine the differential behaviors of BMSCs exhibited by the BCT and BCT@GFs groups, the relative proteins, of osteogenic (Runt-related transcription factor 2, RUNX2), and chondrogenic (sex-determining-region-Y box protein 9, SOX9) were assessed by immunofluorescence (IF) staining. To further study the effect of composite scaffolds on inducing BMSCs to differentiate into tendon, tenogenic relative proteins (Scleraxis, SCX) was examined by IF experiment. Fig. 6J-M showed that the relative expression of RUNX2, SOX9 and SCX proteins were higher in BCT@GFs scaffolds group than those in the control group, indicating the superior osteogenic, chondrogenic, and tenogenic effect for BCT@GFs scaffolds.

The potential osteogenic and chondrogenic differentiation mechanism of BMSCs on biomimetic scaffolds was further examined by quantitative reverse transcription-polymerase chain reaction (qRT-PCR) and Weston blotting (WB) assays. Runt-related transcription factor 2 (RUNX2) is a target of BMP2 and plays an essential role in osteoblast differentiation, which is induced by receptor-activated mitogen-activated protein kinase (MAPK) [66]. As shown in Fig. 7A–D, BCT@GFs scaffolds markedly up-regulated the mRNA expression of BMP2, MAPK (P38) and RUNX2 by releasing BMP2 in BMSCs compared to the BCT scaffold and the control ($p < 0.05$). Moreover, the expression level of p38MAPK protein in BMSCs was evidently up-regulated in BCT@GFs scaffolds compared to the BCT scaffold and the control group ($p < 0.05$) (Fig. 7E and F). The BMP2 released from scaffolds were bound to the receptor, formed a complex at the cell surface, and then activated and phosphorylated p38α/β. Following activation, p38MAPK infiltrated the nucleus, then improved RUNX2 transcription, and induced osteogenic differentiation of BMSCs (Fig. 7O). These results demonstrated that following BMP2 induction, p38MAPK pathways converged at the RUNX2 gene to regulate the differentiation of mesenchymal precursor. Besides, TGF-β3, as a classical chondrogenic inducing factor, exerts a pivotal role in the process of chondrogenesis, predominantly through activation of the drosophila mothers against decapentaplegic protein (Smad) cascade signaling pathway [67,68]. This study had also proved that BCT@GFs scaffold could induce chondrogenic differentiation of BMSCs seeded on scaffolds. As shown in Fig. 7G–K, BCT@GFs scaffolds markedly up-regulated the mRNA expression of recombinant transforming growth factor beta receptor 2 (TGFbr2), common Smad (co-Smad), regulated Smad (R-Smad) and sex-determining-region-Y box protein 9 (SOX9) in BMSCs compared to BCT@GFs ($P < 0.05$) scaffold and the control ($P < 0.01$). In addition, Fig. 7L-N displays that the expression level of the pSmad2/3 protein was significantly improved in BCT@GFs groups compared to the BCT scaffold ($P < 0.01$) and the control ($p < 0.001$), further confirming the activation of TGF-β/Smad signaling pathway. TGF-β3 was bound to the receptor and presented ligands to facilitate signaling. The activated receptor formed a complex with co-Smad (Smad4) by phosphorylating R-Smad (Smad2 and Smad3), and was subsequently translocated to the nucleus and associated with transcription factors to modulate SOX9 expression [69,70] (Fig. 7O). In this study, two essential pathways of osteogenic and chondrogenic differentiation induced by BMP2 and TGF-β3 were confirmed. The two signal transduction pathways played a decisive role in TBI repair. An appropriate concentration of functional factors can promote the process of cell proliferation, differentiation, and matrix synthesis, thereby accelerating the repair and regeneration of the tendon bone interface. Controlling the release rate of functional factors can enable them to function within an appropriate time range, better regulating cellular activity and repair processes. Nonetheless, the role of other signal pathways and the relationship between them remains unclear, which also deserves further research.

3.6. *In vivo* TBI regeneration of different scaffolds

The focus of this study is the integrated repair of tendon, cartilage, and bone at the TBI, thus establishing an avulsion fracture of the posterior calcaneal tubercle model at the insertion area of the rat calcaneus was established to provide a more comprehensive assessment of repair effect of tendon, cartilage, and bone at the interface. Our research provided a feasible repair strategy and a deeper understanding for the repair of avulsion fractures of the posterior calcaneal tubercle in the clinic. The *in vivo* TBI regeneration abilities of BCT, BCT@GFs and Cell + BCT@GFs scaffolds were investigated with a rat Achilles tendon defect model by implantation for 4 and 8 weeks (Fig. S7A), and X-ray, micro computed tomography (micro-CT), histological staining, biomechanical and functional characteristics were performed for analysis (Fig. 8A). After scaffold implantation for 4 and 8 weeks, the specimens were collected for gross morphology, X-ray, micro-CT examination. As depicted in Fig. 8B, the surgical site exhibited no signs of infection or wound

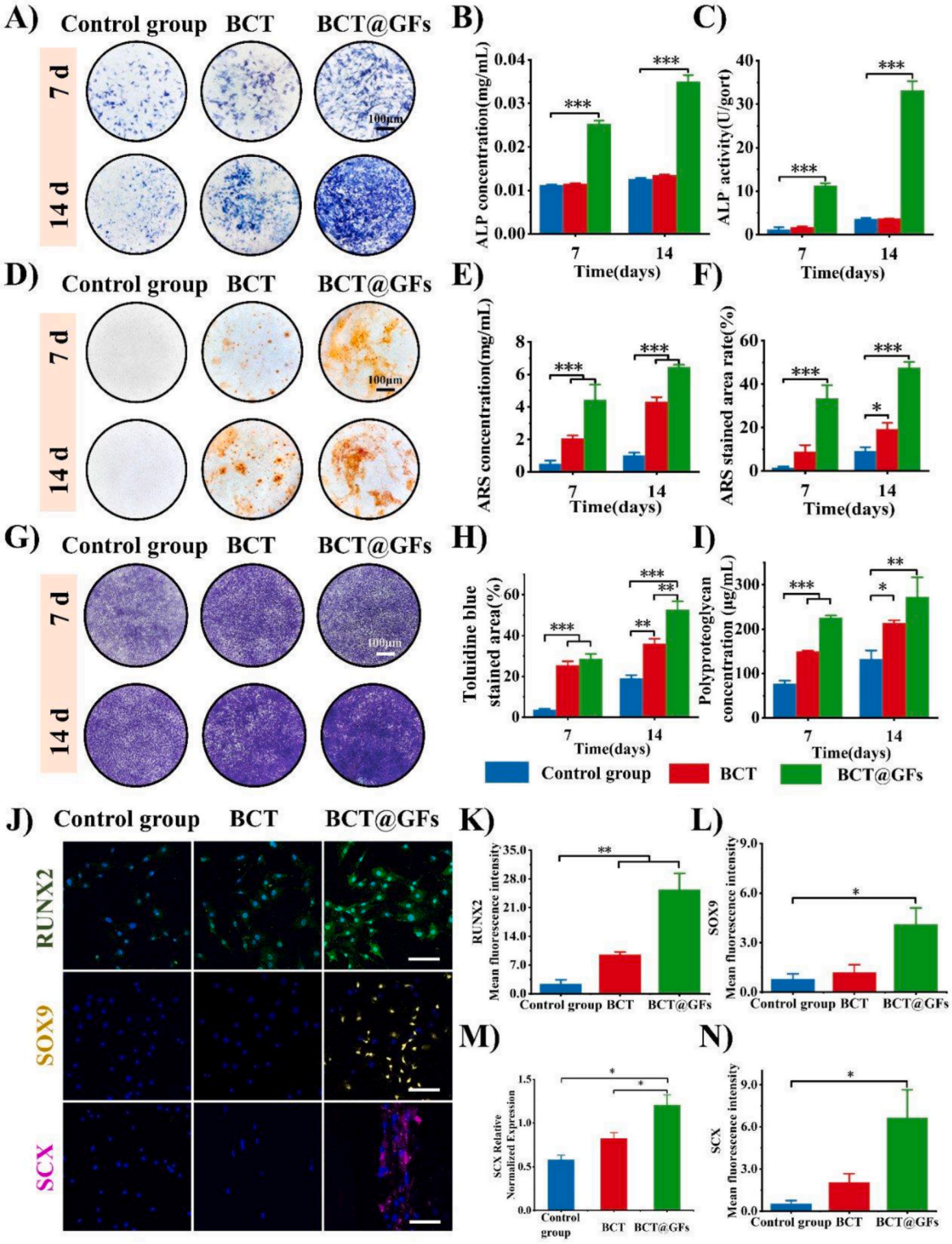

Fig. 6. Cell differentiation on the biomimetic scaffolds. (A–C) ALP staining and colorimetric quantification of ALP activity at 7th day and 14th day after cell seeding. **(D–F)** Mineralization stained with Alizarin red S and colorimetric quantification of ARS. **(G, H)** *Chondrocytes were stained with toluidine blue and* the stained areas were quantified. **(I)** The content of proteoglycan was determined by calcian blue method. **(J)** Immunofluorescence staining images of RUNX2, SOX9, and SCX expression of BMSCs cultured on the BCT and BCT@GFs scaffolds. Scale bar: 100 μm. **(K–M)** Mean fluorescence expression intensity of RUNX2, SOX9, and SCX evaluated on confocal images; **(N)** Differential mRNA expression of tenogenic (SCX) differentiation-related gene. Control group: cells cultured in plates; BCT: cells were seeded on BCT composite scaffold; BCT@GFs: cells were seeded on the composite scaffold loaded with BMP2 and TGF-β3. Each data point represented the mean ± standard deviation (n = 3), statistically significant differences were indicated as *p < 0.05, **P < 0.01 and ***p < 0.001.

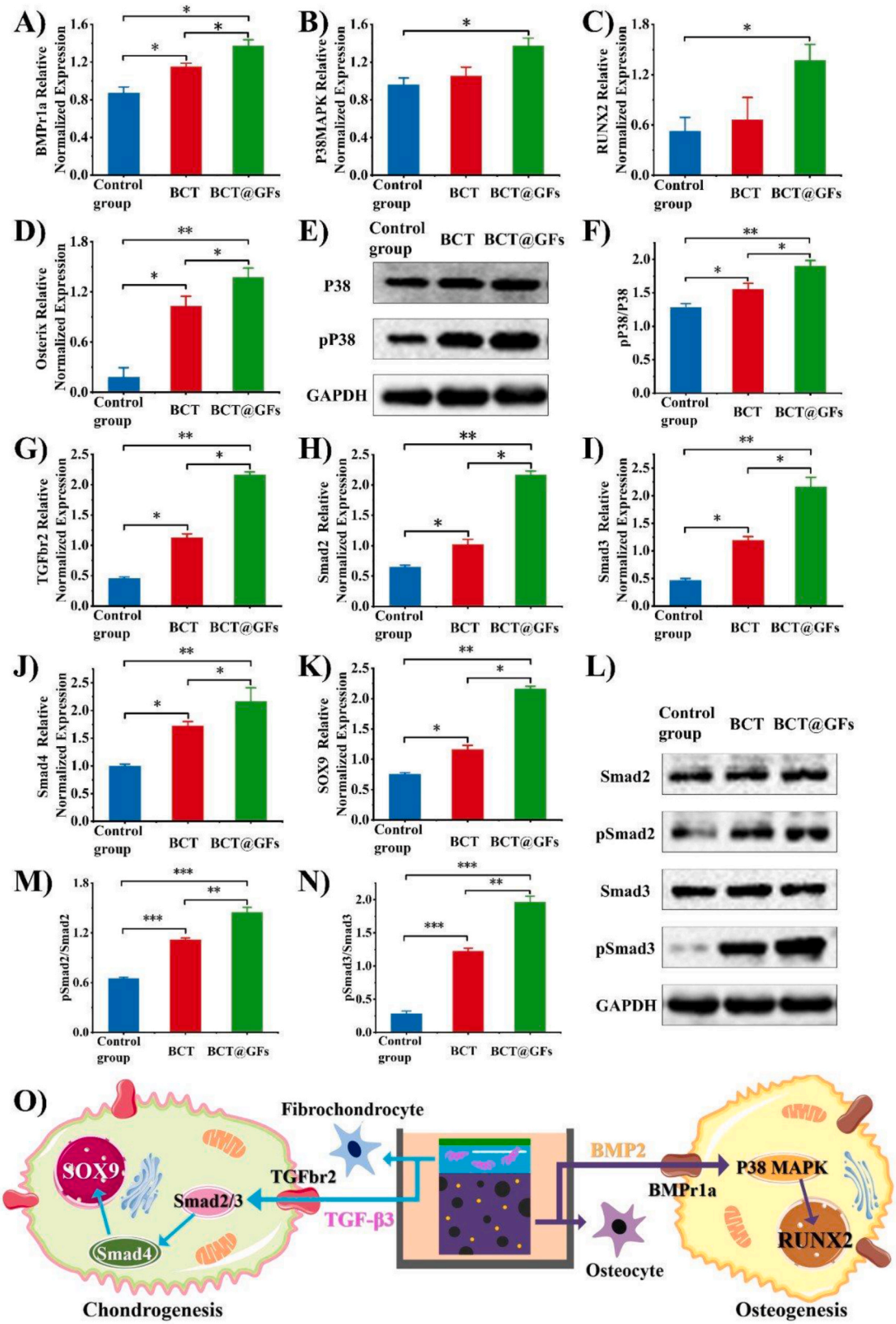

Fig. 7. Cell differentiation mechanism study. (A–D) Differential mRNA expression of mechanism markers of osteogenic pathway (BMPr1a, P38MAPK, RUNX2, Osterix) in the BCT@GFs scaffolds were verified by qRT-PCR analysis. **(E)** Differential protein expression of mechanism markers of osteogenic pathway (P38, pP38) was indicated by western blotting analysis. **(F)** Quantitative analysis of osteogenic mechanism markers by Image J software. **(G–K)** Differential mRNA expression of mechanism markers of chondroblast pathway (TGFbr2, Smad2, Smad3, Smad4, SOX9) in the BCT@GFs scaffolds were verified by qRT-PCR analysis. **(L)** Differential protein expression of mechanism markers of chondroblast pathway (Smad2, pSmad2, Smad3, pSmad3) were indicated by WB analysis. **(M, N)** Quantitative analysis of chondroblast mechanism markers by Image J software. **(O)** Mechanistic insight into the BCT@GFs scaffold-induced osteogenesis and chondrogenesis. Each data point represented the mean ± standard deviation (n = 3), statistically significant differences were indicated as *P < 0.05, **P < 0.01 and ***P < 0.001.

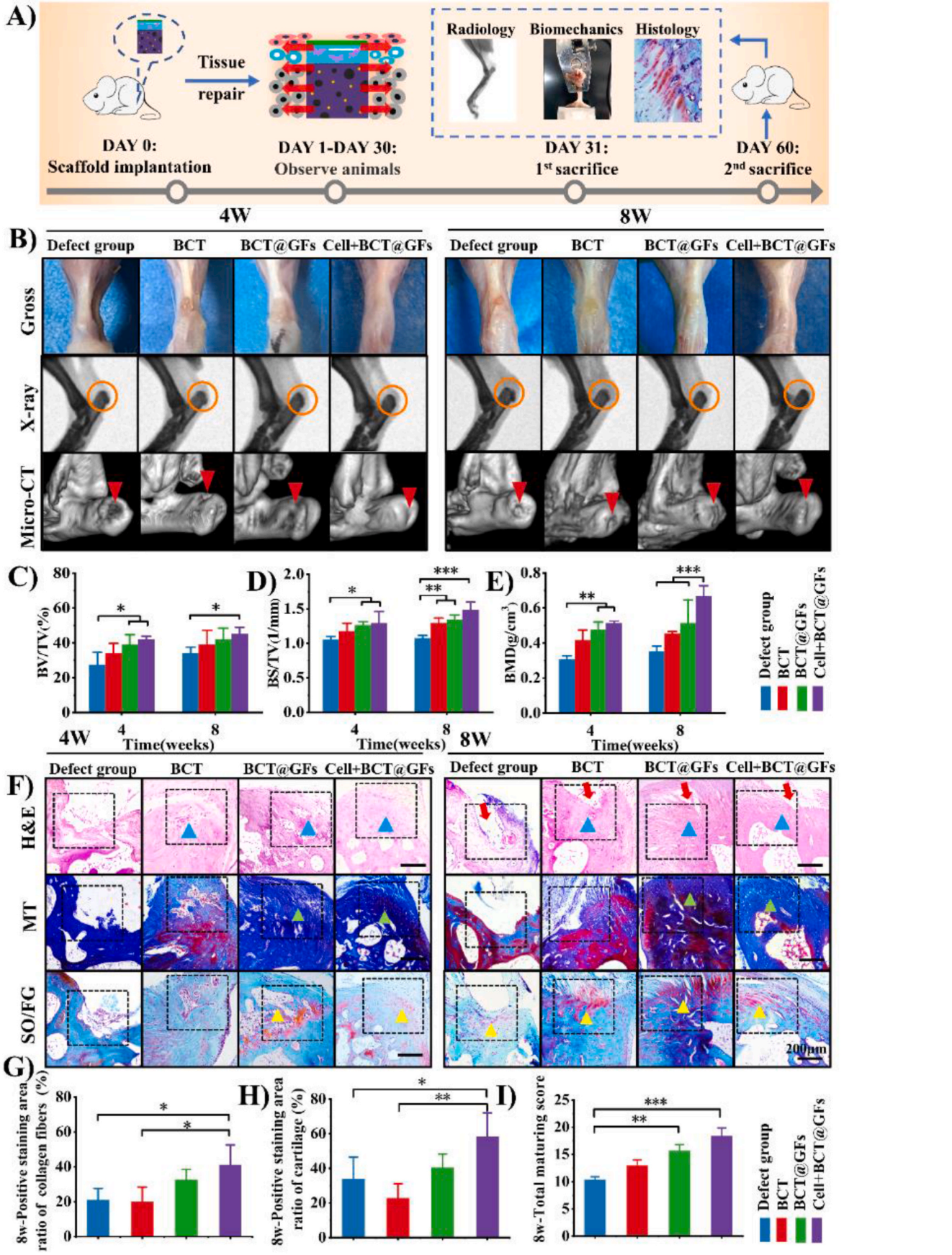

(caption on next page)

Fig. 8. Evaluation of *in vivo* TBI regeneration of different scaffolds and Histological analyses.
(A) Schematic illustration for rat Achilles's tendon defect repaired by scaffold implantation. **(B)** The gross morphologies, X-ray, and micro-CT images in the defect sites after scaffolds implantation for 4 and 8 weeks. The defect sites without scaffold implantation served as the control group. Orange circles labeled new bone and red arrows labeled new bone. **(C–E)** Bone volume fractions (BV/TV) bone surface fractions (BS/TV), and bone mineral density (BMD)analysis determined by micro-CT at 8th weeks. **(F)** Histological observation of TBI regeneration at the defect areas after scaffolds implantation for 4 and 8 weeks by H&E, Masson's trichrome and Safranin-O/Fast green (SO/FG) staining (magnification × 100, Scale bar: 200 μm). Blue arrows labeled the new bone, green arrows labeled the collagen fibers, red arrows labeled the undegraded scaffolds, and yellow arrows labeled cartilage. **(G, H)** Quantitative analysis of collagen fibers, cartilage positive staining area ratio at 8th week. **(I)** The histological total maturing scores of TBI defect areas after scaffolds implantation for 8 weeks. Each data point represented the mean ± standard deviation (n = 3), statistically significant differences were indicated as *P < 0.05, **P < 0.01 and ***P < 0.001.

dehiscence in all rats. After 4 and 8 weeks of implantation, the surface of regenerated TBI tissue in the BCT@GFs and Cell + BCT@GFs groups was smoother than that in the BCT and blank control groups. X-ray and micro-CT imaging revealed that the defect areas at 8th week were smaller relative to the defect scope at 4th week for all the groups. However, the untreated defect group still presented a larger area of TBI defect compared with the scaffold groups, which could be attributed to poorly regenerated calcaneus, displaying a limited capacity for self-healing. Interestingly, the defect region shrunk sharply and was almost filled with new bone in the Cell + BCT@GFs group, indicating rapid new bone regeneration. Moreover, the quantitative results of the ratio of new bone volume to total volume (BV/TV) and bone surface fractions to total volume (BS/TV), bone mineral density (BMD) further established that scaffolds implantation further induced new bone formation compared to the scaffold-free treatment (Fig. 8C–E). More importantly, at 4th week, new bone formation in the BCT@GFs and Cells + BCT@GFs groups was significantly higher than that of the control group ($p < 0.01$), while there were no significant differences between the BCT@GFs and Cells + BCT@GFs groups ($p > 0.05$). At 8th week, the BS/TV and BMD of the Cells + BCT@GFs group (1.49 ± 0.09 mm^{-1}, 0.68 ± 0.04 g/cm^3) were significantly higher than that of the other three groups ($p < 0.001$). Then, we calculated that the degradation rates of BCT, BCT@GFs and Cell + BCT@GFs *in vivo* at 8th week were 42.00 ± 9.09 %, 45.00 ± 10.23 %, 39.33 ± 7.85 %, respectively. These results showed that the implanted scaffold could effectively degrade *in vivo* without long-term retention, which guaranteed a sustained release of the loaded drugs. Collectively, these results demonstrated that the Cells + BCT@GFs scaffold induced more newly-formed bone and exhibited the optimal performance on TBI regeneration, mainly attributed to the enhanced osteogenic effect. But the lack of μCT should be considered as a limiting factor in our study. Although, compared with micro-CT, μCT has higher resolution and better imaging effect, and can provide more accurate and detailed sample structure information [3, 71], micro-CT, which is more economical and common than μCT, also can provide reliable data and support the conclusion, which also has been verified in other researchers' studies [6].

In order to examine verify the scaffolds-mediated TBI repair, cross sections of defects were analyzed by hematoxylin and eosin (H&E), Masson's trichrome (MT), and safranin-O/fast green (SO/FG) staining. As shown in the H&E staining (Fig. 8F), the area pointed by the arrow is the undegraded scaffold area. With the degradation of the scaffold, some tissues and cells gradually grow into the implanted scaffold and occupy the scaffold area. The result showed no obvious necrosis or inflammatory response in the implanted groups at 8th week post-operation (Fig. 8F), indicating the favorable biocompatibility of these scaffolds. Moreover, considerable fibrous tissue formation, inadequate bone reconstruction and a large area of void space were observed in the control group. Conversely, more new bone formation was observed in scaffold implanted groups, especially for BCT@GFs and Cells + BCT@GFs groups. Results of MT and SO/FG staining corroborated that the newly formed collagen fibers and cartilage were higher in the TBI in BCT@GFs and Cells + BCT@GFs groups than those in the control group, which was more beneficial to forming a continuous transition between neo-cartilage and subchondral bone. The statistical data based on the staining observation at 4 and 8 weeks after the operation are shown in Figs. S7B–D and Fig. 8G–I, respectively. Notably, the area ratio of collagen fibers to cartilage positive staining of the Cells + BCT@GFs group was 42.67 ± 5.40 % and 58.38 ± 13.69 % at 8th week, which was significantly better compared with the control group (Fig. 8G and H). The total histological scores of BCT@GFs (15.67 ± 0.94, $p < 0.01$) and Cells + BCT@GFs (18.33 ± 1.24, $p < 0.001$) groups were remarkably higher than the control group (Fig. 8I), indicating improved cellular and fiber orientation, fiber maturation, and TBI remodeling in groups of BCT@GFs and Cells + BCT@GFs. These results demonstrated that the Cells + BCT@GFs group, exhibited superior TBI repairing outcomes and evidently improved structure of TBI, such as fibrocartilage formation and collagen organization, without any further immune response. These results indicated that the biomimetic scaffold effectively simulated the transitional structure of TBI and BMSCs synthesized specific matrices according to the specific region in the early stage of TBI repair [72].

3.7. Function assessment of TBI regeneration after scaffolds implantation

After an injury, the mechanical strength of regenerated tissue usually decreases since the strong structure of normal TBI is substituted by weak fibrous scar tissues [73]. Although the structure of defected TBI could somewhat be promoted by scaffolds, the failure rate of TBI healing was still high due to the low failure load. Therefore, mechanical properties at the TBI are a key indicator to judging the healing quality of the TBI function. For functional evaluation of TBI regeneration after scaffolds implantation, the biomechanical properties of Achilles's tendon-muscle and attached calcaneus complex are measured by mechanical tensile testing examination (Fig. 9A). Representative force–displacement curves at 4th and 8th week were shown in Fig. 9B and C. In this experiment, a series of biomechanical property characterization data results were obtained by analyzing the force–displacement curves. As shown in Fig. 9D and E, the cross-sectional area and young's modulus of the insertion site presented no significant difference between the normal tendon tissue and all scaffold implanted groups ($p > 0.05$). The results of the maximum load are shown in Fig. 9F and the result exposed that the Cells + BCT@GFs group exhibited the highest maximum load among all scaffold implanted groups, very close to normal tendon tissue. The maximum stress of the Cells + BCT@GFs groups was also considerably higher than that of the other group, which reached 57.31 % of the normal tendon (Fig. 9G). Furthermore, for the energy to failure, there was no significant difference between the Cells + BCT@GFs group (224.54 ± 82.46 N*mm) and the normal tendon (276.66 ± 46.12 N*mm) at 4th week (Fig. 9H). Strikingly, the energy to failure of the Cells + BCT@GFs group was higher than that of the normal tendon at 8th week, indicating markedly improved TBI regeneration and satisfactory repair effects. These results demonstrated that the main mechanical functions of TBI under the Cells + BCT@GFs scaffold treatment were almost recovered at the early phase and very close to the normal TBI, which undoubtedly would be beneficial to following TBI regeneration in the later phase and finally achieving successful therapeutic outcomes.

TBI healing is one of the most challenging factors affecting clinical outcomes for patients after surgery, since TBI is highly anisotropic and consists of mechanical, compositional, and hierarchical structures with tendon and bone-like properties. Previous studies reported single phase scaffolds had limitations in representing the complex structure of TBI, which couldn't effectively promote regenerate of the structural and

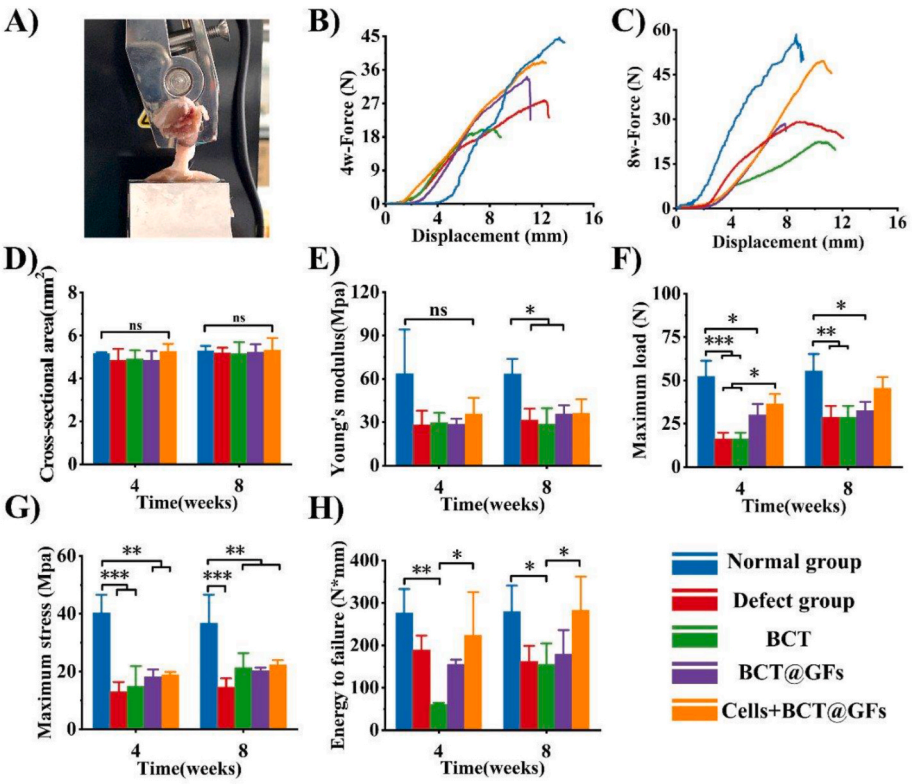

Fig. 9. Biomechanical study for TBI after repair. (A) Biomechanical testing of the Achilles's tendon-muscle and attached calcaneus complex at 4th and 8th week after enthesis reconstruction surgery. The load-to-failure of Achilles's tendon-muscle and attached calcaneus complex tested enthesis. **(B, C)** Force-displacement curve. **(D)** Cross-sectional area. **(E)** Young's modulus. **(F)** Maximum load. **(G)** Maximum stress. **(H)** Energy to failure. Each data point represented the mean ± standard deviation (n = 3), statistically significant differences were indicated as ns > 0.05, *p < 0.05, **p < 0.01 and ***p < 0.001.

gradients of TBI and exhibit poorer performance [74–76]. Different from the traditional scaffolds, this study designed a hierarchically-structured scaffold on basis of the "tissue-inducing biomaterials" theory. The biomimetic scaffold composed of three layers, including PLA fibers, collagen/BMSCs/TGF-beta3 loaded hydrogel, and BMP2/n-HA loaded PLGA, to mimic tendon-bone interface (tendon, cartilage, and bone, respectively), thereby reducing stress concentration and then enhancing the tendon graft integration into bone. Results indicated the scaffold achieved good repair effects, and it expected to be applied in clinical practice in the future. Besides, BTI injury repair still was a challenge because of the low bioactivity of the tissue-engineered scaffolds [77]. Therefore, to overcome these shortcomings, the scaffold with hierarchical structural composition, physicochemical properties and graded inductivity was fabricated according to the composition of the heterogeneous structure and function of natural TBI, which combined scaffold materials, seed cells, and cytokine mediated strategy as a system for overall design of TBI reconstruction from various aspects. Accordingly, including these spatially-regulated biochemical signals into the composite promotes the regional regulation of cell fate, hence achieving bionic engineering scaffolds that are closer to natural tissues. Therefore, the design of this scaffold provided a new idea for the repair of TBI, and laid an experimental foundation for the regeneration of such heterogeneous tissues. The scaffold was expected to be widely used in clinical applications, providing a new treatment for TBI healing, and a reference for regeneration of other heterogeneous tissues.

4. Conclusion

In summary, multiple-layer biomimetic scaffolds loaded with growth factors were designed based on the principles of the "tissue-inducing biomaterials" theory, mimicking the functions and characteristics of the natural tendon-bone interface microstructure to meet the demands of TBI regeneration. The hierarchical scaffolds were developed with three layers: PLGA/nHA porous scaffolds loaded with BMP2-gelatin$_{mp}$ to simulate the native bone phase, Alg/Col-I hydrogels loaded with TGF-β3 to simulate the native cartilage phase, and the PLLA oriented fibers to simulate the native tendon phase, respectively. The hierarchical microstructures not only endowed the scaffold with continuous gradual composition and matrix material properties for matching the regional biophysical characteristics of natural TBI tissues but also enabled BMSCs to proliferate and distribute uniformly inside the scaffold at a highly viable, proliferative, and migratory rate. Additionally, osteogenesis and chondrogenesis differentiation of BMSCs were promoted through controlled delivery of BMP2 and TGF-β3 in the distinct bone and cartilage phases of the scaffold. This study experimentally proved that the hierarchical scaffolds could induce osteogenic and chondrogenic differentiation of BMSCs through the MAPK and Smad pathways. Moreover, the biomimetic scaffolds seeded with cells could effectively accelerate the formation of a mechanically functional tendon-bone interface in rat Achilles tendon defect for enhanced osteogenic, chondrogenesis, and tenogenic performance. Collectively, a novel hierarchical scaffold was designed and provided a structurally and compositionally adequate microenvironment for TBI regeneration, which were a prospective strategy for TBI regeneration. The limitation of this study is that the bonding force of between tendon and bone and the fate of seeded cells after implantation were not investigated. It was unclear whether BMSCs survived after transplanted in the defected tissue. Further research should focus on the cellular activity of BMSCs implanted, which may play an important role in TBI repair.

Compliance with ethical standards

Animal care and experiments were performed according to the principles of Ethics Committee of Chongqing Medical University. All

protocols in this study were approved by the Ethics Committee of Chongqing Medical University (No. 2022039).

Declaration of competing interest

The authors declare no conflict of interest that could have appeared to influence the work reported in this paper.

Acknowledgements

This work was financially supported by the National Natural Science Foundation of China (32371415, 32370985, 82202459), Natural Science Foundation of Chongqing Municipality (CSTB2023NSCQ-MSX0307, CSTB2022NSCQ-MSX0153), Program for Youth Innovation in Future Medicine from Chongqing Medical University (W0055, W0100), Innovation and Business Projects of Chongqing City (SRIEP202194).

Appendix A. Supplementary data

Supplementary data to this article can be found online at https://doi.org/10.1016/j.jot.2024.07.007.

References

[1] Cottrell MA, Russell TG. Telehealth for musculoskeletal physiotherapy. Musculoskelet. Sci Pract 2020;48:102193.
[2] Rothrauff BB, Pauyo T, Debski RE, Rodosky MW, Tuan RS, Musahl V. The rotator cuff organ: integrating developmental biology, tissue engineering, and surgical considerations to treat chronic massive rotator cuff tears. Tissue Eng Part B 2017;23(4):318–35.
[3] Rossetti L, Kuntz LA, Kunold E, Schock J, Müller KW, Grabmayr H, et al. The microstructure and micromechanics of the tendon-bone insertion. Nat Mater 2017;16(6):664–70.
[4] Ostrovidov S, Salehi S, Costantini M, Suthiwanich K, Ebrahimi M, Sadeghian RB, et al. 3D bioprinting in skeletal muscle tissue engineering. Small 2019;15(24):1805530.
[5] Cai Y, Zhang C, Lin X. Efficacy of platelet-rich plasma in arthroscopic repair of full-thickness rotator cuff tears: a meta-analysis. J Shoulder Elbow Surg 2015;24(12):1852–9.
[6] Rahmati M, Stötzel S, ElKhassawna T, Mao C, Ali A, Vaughan JC, et al. Intrinsically disordered peptides enhance regenerative capacities of bone composite xenografts. Mater Today 2022;52:63–79.
[7] Li X, Cheng R, Sun Z, Su W, Pan G, Zhao S, et al. Flexible bipolar nanofibrous membranes for improving gradient microstructure in tendon-to-bone healing. Acta Biomater 2017;(61):204.
[8] Wang D, Zhang X, Huang S, Liu Y, Fu SC, Mak KL. Engineering multi-tissue units for regenerative medicine: bone-tendon-muscle units of the rotator cuff. Biomaterials 2021;272:120789.
[9] Lei T, Zhang T, Ju W, Chen X, Heng BC, Shen W, et al. Biomimetic strategies for tendon/ligament-to-bone interface regeneration. Bioact Mater 2021;6:2491–510.
[10] Ide J, Tokunaga T. Rotator cuff tendon-to-bone healing at 12 months after patch grafting of acellular dermal matrix in an animal model. J Orthop Sci 2017;23(2):S735476093.
[11] Cao Y, Yang D, Zhao D, Li Y, Cheong SS, Han D, et al. Three-dimensional printed multiphasic scaffolds with stratified cell-laden gelatin methacrylate hydrogels for biomimetic tendon-to-bone interface engineering. J Orthop Translat 2020;23:89–100.
[12] Patel S, Gualtieri AP, Lu HH, Levine WN. Advances in biologic augmentation for rotator cuff repair. Ann NY Acad Sci 2016;1383(1):97–114.
[13] Calejo I, Costa-Almeida R, Reis RL, Gomes ME. A physiology-inspired multifactorial toolbox in soft-to-hard musculoskeletal interface tissue engineering. Trends Biotechnol 2020;38(1):83–98.
[14] Tarafder S, Park GY, Felix J, Lee CH. Bioadhesives for musculoskeletal tissue regeneration. Acta Biomater 2020;117:77–92.
[15] Chen P, Cui L, Chen G, You T, Li W, et al. The application of BMP-12-overexpressing mesenchymal stem cells loaded 3D-printed PLGA scaffolds in rabbit rotator cuff repair. Int J Biol Macromol 2019;138:79–88.
[16] Seuba J, Maire E, Adrien J, Meille S, Deville S. Mechanical properties of unidirectional, porous polymer/ceramic composites for biomedical applications. Open Ceramics 2021;8:100195.
[17] Zou L, Zhang Y, Liu X, Chen J, Zhang Q. Biomimetic mineralization on natural and synthetic polymers to prepare hybrid scaffolds for bone tissue engineering. Colloids Surf B Biointerfaces 2019;178:222–9.
[18] Xavier JR, Thakur T, Desai P, Jaiswal MK, Sears N, Cosgriff-Hernandez E, et al. Bioactive nanoengineered hydrogels for bone tissue engineering: a growth-factor-free approach. ACS Nano 2015;9(3):3109–18.
[19] Yang S, Shi X, Li X, Wang J, Wang Y, Luo Y. Oriented collagen fiber membranes formed through counter-rotating extrusion and their application in tendon regeneration. Biomaterials 2019;207:61–75.
[20] Sharma P, Maffulli N. Tendon injury and tendinopathy: healing and repair. J Bone Joint Surg Am 2005;87(1):187–202.
[21] Docheva D, Müller SA, Majewski M, Evans CH. Biologics for tendon repair. Adv Drug Deliv Rev 2015;84:222–39.
[22] Yang R, Li G, Zhuang C, Yu P, Ye T, Zhang Y, et al. Gradient bimetallic ion-based hydrogels for tissue microstructure reconstruction of tendon-to-bone insertion. Sci Adv 2021;7(26):3816.
[23] Shi W, Sun M, Hu X, Ren B, Cheng J, Li C. Structurally and functionally optimized silk-fibroin-gelatin scaffold using 3D printing to repair cartilage injury in vitro and in vivo. Adv Mater 2017;29(29):1701089.1–7.
[24] Huang Y, Lin Y, Chen C, Hsieh Y, Liaw C, Huang S, et al. Thermosensitive chitosan-gelatin-glycerol phosphate hydrogels as collagenase carrier for tendon-bone healing in a rabbit model. Polymers 2020;12(2):436.
[25] Tu T, Shen Y, Wang X, Zhang W, Zhou G, Zhang Y, et al. Tendon ECM modified bioactive electrospun fibers promote MSC tenogenic differentiation and tendon regeneration. Appl Mater Today 2020;18:100495.
[26] Long C, Wang Z, Legrand A, Chattopadhyay A, Chang J, Fox PM. Tendon tissue engineering: mechanism and effects of human tenocyte coculture with adipose-derived stem cells. J Hand Surg Am 2018;43(2):181–3.
[27] Xie J, Li X, Lipner J, Manning CN, Schwartz AG, Thomopoulos S, et al. "Aligned-to-random" nanofiber scaffolds for mimicking the structure of the tendon-to-bone insertion site. Nanoscale 2010;2(6):923.
[28] Sundaram MN, Deepthi S, Mony U, Shalumon KT, Chen J, Jayakumar R. Chitosan hydrogel scaffold reinforced with twisted poly(L-lactic acid) aligned microfibrous bundle to mimic tendon extracellular matrix. Int J Biol Macromol 2019;122:37–44.
[29] Wu S, Zhou R, Zhou F, Streubel PN, Chen S, Duan B. Electrospun thymosin beta-4 loaded PLGA/PLA nanofiber/microfiber hybrid yarns for tendon tissue engineering application. Mater Sci Eng C 2020;106:110268.
[30] Terzopoulou Z, Zamboulis A, Koumentakou I, Michailidou G, Noordam MJ, Bikiaris DN. Biocompatible synthetic polymers for tissue engineering purposes. Biomacromolecules 2022;23(5):1841–63.
[31] Chen FM, Min Z, Wu ZF. Toward delivery of multiple growth factors in tissue engineering. Biomaterials 2010;31(24):6279–308.
[32] Rezwan K, Chen Q, Blaker Z, Boccaccini JJ. Biodegradable and bioactive porous polymer/inorganic composite scaffolds for bone tissue engineering. Biomaterials 2006;27(18):3413–31.
[33] Kim JH, Oh SH, Min HK, Lee JH. Dual growth factor-immobilized asymmetrically porous membrane for bone to tendon interface regeneration on rat patellar tendon avulsion model. J Biomed Mater Res 2018;106(1):115–25.
[34] Zhou M, Lozano N, Wychowaniec JK, Hodgkinson T, Richardson SM, Kostarelos K, et al. Graphene oxide: a growth factor delivery carrier to enhance chondrogenic differentiation of human mesenchymal stem cells in 3D hydrogels. Acta Biomater 2019;96:271–80.
[35] Yadin D, Knaus P, Mueller TD. Structural insights into BMP receptors: specificity, activation and inhibition. Cytokine Growth Factor Rev 2016;27:13–34.
[36] Galatz L, Rothermich S, Vanderploeg K, Petersen B, Sandell L, Thomopoulos S. Development of the supraspinatus tendon to bone insertion: localized expression of extracellular matrix and growth factor genes. J Orthop Res 2007;25(12):1621–8.
[37] Wei B, Wang C, Yan C, Tang B, Yu X, Zhang H, et al. Osteoprotegerin/bone morphogenetic protein 2 combining with collagen sponges on tendon-bone healing in rabbits. J Bone Miner Metabol 2020;38(4):432–41.
[38] Harris E, Liu Y, Cunniffe G, Morrissey D, Carroll S, Mulhall K, et al. Biofabrication of soft tissue templates for engineering the bone-ligament interface. Biotechnol Bioeng 2017;114(10):2400–11.
[39] Yonemitsu R, Tokunaga T, Shukunami C, Ideo K, Mizuta H. Fibroblast growth factor 2 enhances tendon to bone healing in a rat rotator cuff repair of chronic tears. Am J Sports Med 2019;47(359):2048790351.
[40] Nickel J, Mueller TD. Specification of BMP signaling. Cells 2019;8(12).
[41] Deng L, Huang L, Guo Q, Shi X, Xu K. Creb1 and smad3 mediate TGF β3 induced smad7 expression in rat hepatic stellate cells. Mol Med Rep 2017;16(6):8455–62.
[42] Thomopoulos S, Kim HM, Silva MJ, Ntouvali E, Manning CN, Potter R, et al. Effect of bone morphogenetic protein 2 on tendon to bone healing in a canine flexor tendon model. J Orthop Res 2012;30(11):1702–9.
[43] Kim HM, Galatz LM, Das R, Havlioglu N, Rothermich SY, Thomopoulos S. The role of transforming growth factor beta isoforms in tendon to bone healing. Connect Tissue Res 2011;52(2):87–98.
[44] Reifenrath J, Wellmann M, Kempfert M, Angrisani N, Welke B, Gniesmer S, et al. TGF-β3 loaded electrospun polycaprolacton fibre scaffolds for rotator cuff tear repair: an in vivo study in rats. Int J Mol Sci 2020;21(3):1046.
[45] Kang F, Yi QY, Gu PC, Dong YH, Zhang ZY, Zhang LJ, et al. Controlled growth factor delivery system with osteogenic-angiogenic coupling effect for bone regeneration. J Orthop Transl 2021;31:110–25.
[46] Ide J, Kikukawa K, Hirose J, Iyama K, Sakamoto H, Mizuta H. The effects of fibroblast growth factor-2 on rotator cuff reconstruction with acellular dermal matrix grafts. Arthroscopy 2009;25(6):608–16.
[47] Lipski AM, Pino CJ, Haselton FR, Chen IW, Shastri VP. The effect of silica nanoparticle-modified surfaces on cell morphology, cytoskeletal organization and function. Biomaterials 2008;29(28):3836–46.
[48] Olivares-Navarrete R, Rodil SE, Hyzy SL, Dunn GR, Almaguer-Flores A, Schwartz Z, et al. Role of integrin subunits in mesenchymal stem cell differentiation and osteoblast maturation on graphitic carbon-coated microstructured surfaces. Biomaterials 2015;51:69–79.

[49] Kim BS, Kim EJ, Choi JS, Jeong JH, Jo CH, Cho YW. Human collagen-based multilayer scaffolds for tendon to bone interface tissue engineering. J Biomed Mater Res, Part A 2015;102(11):4044–54.
[50] Ruys A. Dental tissue scaffold, and other specialized biomedical applications of alumina. Alumina Ceramics 2019:123–37.
[51] Tienen T, Heijkants R, Buma P, Groot J, Veth R. Tissue ingrowth and degradation of two biodegradable porous polymers with different porosities and pore sizes. Biomaterials 2022;23(8):1731–8.
[52] Prabhath A, Vernekar VN, Sanchez E, Laurencin CT. Growth factor delivery strategies for rotator cuff repair and regeneration. Int J Pharm 2018:S1850503581.
[53] Kovacevic D, Rodeo SA. Biological augmentation of rotator cuff tendon repair. Clin Orthop Relat Res 2008;3:622–33.
[54] Chen G, Deng C, Li YP. TGF-β and BMP signaling in osteoblast differentiation and bone formation. Int J Biol Sci 2012;8(2):272–88.
[55] Deng L, Huang L, Guo Q, Shi X, Xu K. Creb1 and smad3 mediate TGF-β3-induced smad7 expression in rat hepatic stellate cells. Mol Med Rep 2017;16(6):8455–62.
[56] Ai-Aql ZS, Alagl AS, Graves DT, Gerstenfeld LC, Einhorn TA. Molecular mechanisms controlling bone formation during fracture healing and distraction osteogenesis. J Dent Res 2008;87(2):107–18.
[57] Garrison KR, Donell S, Ryder J, Shemilt I, Mugford M, Harvey I, et al. Clinical effectiveness and cost-effectiveness of bone morphogenetic proteins in the non-healing of fractures and spinal fusion: a systematic review. Health Technol Assess 2007;11(30):1–150.
[58] Galatz L, Rothermich S, Vanderploeg K, Petersen B, Sandell L, Thomopoulos S. Development of the supraspinatus tendon to bone insertion: localized expression of extracellular matrix and growth factor genes. J Orthop Res 2010;25(12):1621–8.
[59] Ker DF, Wang D, Behn AW, Wang ET, Zhang X, Zhou BY, et al. Functionally graded, bone- and tendon-like polyurethane for rotator cuff repair. Adv Funct Mater 2018; 28(20):1707107.
[60] Liu H, Yang L, Zhang E, Zhang R, Cai D, Zhu S, et al. Biomimetic tendon extracellular matrix composite gradient scaffold enhances ligament-to-bone junction reconstruction. Acta Biomater 2017;(56):129–40.
[61] Yin Z, Chen X, Song HX, Hu JJ, Tang QM, Zhu T, et al. Electrospun scaffolds for multiple tissues regeneration in vivo through topography dependent induction of lineage specific. Biomaterials 2015;(44):173–85.
[62] Liu S, Liu Y, Jiang L, Li Z, Lee S, Liu C, et al. Recombinant human bmp-2 accelerates the migration of bone marrow mesenchymal stem cells via the CDC42/ PAK1/LIMK1 pathway in vitro and in vivo. Biomater Sci 2019;7(1):362–72.
[63] Du Y, Guo JL, Wang J, Mikos AG, Zhang S. Hierarchically designed bone scaffolds: from internal cues to external stimuli. Biomaterials 2019;218:119334.
[64] Adam J, Shamik SE, Sweeney HL. Matrix elasticity directs stem cell lineage specification. Cell 2006:677–89.
[65] Dagher E, Hays PL, Kawamura S, Godin J, Deng X, Rodeo SA. Immobilization modulates macrophage accumulation in tendon-bone healing. Clin Orthop Relat Res 2009;467(1):281–7.
[66] Afzal F, Pratap J, Ito K, Ito Y, Stein JL, Wijnen A, et al. Smad function and intranuclear targeting share a RUNX2 motif required for osteogenic lineage induction and BMP2 responsive transcription. J Cell Physiol 2005;204(1):63–72.
[67] Tang QO, Shakib K, Heliotis M, Tsiridis E, Mantalaris A, Ripamonti U, et al. TGF-beta3: a potential biological therapy for enhancing chondrogenesis. Expert Opin Biol Ther 2009;9(6):689–701.
[68] Gonzalez-Fernandez T, Tierney EG, Kelly DJ, O'Brien FJ. Gene delivery of TGF-beta 3 and BMP2 in an MSC-laden alginate hydrogel for articular cartilage and endochondral bone tissue engineering. Tissue Eng Part A 2016;10:776–87.
[69] Furumatsu T, Ozaki T, Asahara H. Smad3 activates the SOX9-dependent transcription on chromatin. Int J Biochem Cell Biol 2008;41(5):1198–204.
[70] Moustakas A, Souchelnytskyi S, Heldin CH. Smad regulation in TGF-beta signal transduction. J Cell Sci 2022;114(24):4359–69.
[71] Ding SL, Xin L, Zhao XY, Wang KT, Wei X, Gao ZL, et al. Microcarriers in application for cartilage tissue engineering: recent progress and challenges. Bioact Mater 2022;17:81–108.
[72] Cholas R, Padmanabhan SK, Gervaso F, Udayan G, Monaco G, Sannino A, et al. Scaffolds for bone regeneration made of hydroxyapatite microspheres in a collagen matrix. Mater Sci Eng C 2016;63:499–505.
[73] Mariana L, Rui MA, Raquel CA, Rui LR, Manuela EG. 3D mimicry of native tissue fiber architecture guides tendon derived cells and adipose stem cells into artificial tendon constructs. Small 2017:1700689.
[74] Crapo PM, Gilbert TW, Badylak SF. An overview of tissue and whole organ decellularization processes. Biomaterials 2011;32:3233–43.
[75] Woon CY, Farnebo S, Schmitt T, Kraus A, Megerle K, Pham H, et al. Human flexor tendon tissue engineering: revitalization of biostatic allograft scaffolds. Tissue Eng Part A 2012;18:2406–17.
[76] Ozasa Y, Amadio PC, Thoreson AR, An KN, Zhao C. Repopulation of intrasynovial flexor tendon allograft with bone marrow stromal cells: an ex vivo model. Tissue Eng Part A 2014;20:566–74.
[77] Yongchun Z, Shanshan X, Yifu T, Xiaoning L, Yong C, et al. Effect of book-shaped acellular tendon scaffold with bone marrow mesenchymal stem cells sheets on bone-tendon interface healing. J Orthop Translat 2021:26162–70.